



MOX-Report No. 06/2015

**Space-time adaptive hierarchical model reduction for
parabolic equations**

Perotto, S.; Zilio, A.

MOX, Dipartimento di Matematica
Politecnico di Milano, Via Bonardi 9 - 20133 Milano (Italy)

mox-dmat@polimi.it

<http://mox.polimi.it>

Space-time adaptive hierarchical model reduction for parabolic equations

Simona Perotto[‡] and Alessandro Zilio[♭]

February 10, 2015

[‡] MOX– Modellistica e Calcolo Scientifico
Dipartimento di Matematica, Politecnico di Milano
Piazza Leonardo da Vinci 32, 20133 Milano, Italy

[♭] Centre d'Analyse et de Mathématique Sociales,
École des Hautes Études en Sciences Sociales,
190-198 Avenue de France, 75244 Paris CEDEX 13, France
`simona.perotto@polimi.it, azilio@ehess.fr`

Keywords: model reduction, validation and verification, a posteriori modeling error analysis, mesh adaptivity, space-time finite elements, modal expansion

AMS Subject Classification: 78M34, 65M15, 65T40, 65M60

Abstract

We formalize the pointwise HiMod approach in an unsteady setting, by resorting to a model discontinuous in time, continuous and hierarchically reduced in space (c[M(**M**)G(*s*)]-dG(*q*) approximation). The selection of the modal distribution and of the space-time discretization is automatically performed via an *a posteriori* analysis of the global error. The results of the numerical verification confirm the robustness of the proposed adaptive procedure in terms of accuracy as well as of sensitivity with respect to the goal quantity. The validation results in the groundwater experimental setting are actually more than satisfying, with an improvement in the concentration predictions by means of the adaptive HiMod approximation.

1 Background

The extensive use of scientific computing in many fields of science and engineering requires more and more frequently to reach a compromise between modeling reliability and computational efficiency [1]. This goal is currently

pursued in the literature via the set up of two complementary methodologies, i.e., *surrogate solutions* and *surrogate models*. Surrogate solutions are generally formalized with a reduction of the size of the finite dimensional solution, as in the Reduced Basis approach [2], or in the Proper Orthogonal Decomposition (POD) [3] and Proper Generalized Decomposition (PGD) methods [4].

Surrogate models directly replace the reference model via a simplified formulation as with a geometric multiscale modeling [5, 6] or with compressed sensing [7]. This is usually accomplished by taking advantage of specific features of the problem at hand, such as a prevalent direction in the involved dynamics rather than in the geometry of the computational domain. This is exactly the criterion exploited to settle the Hierarchical Model (HiMod) reduction proposed in [8, 9]. The HiMod technique derives enriched 1D surrogate models to describe phenomena characterized by a leading dynamics albeit in the presence of locally significant transverse features. In particular, the description properties of purely 1D models are enhanced by keeping track of the transverse dynamics in the reduced model. This is achieved by enriching a finite element discretization of the mainstream with a modal representation of the secondary dynamics. This strategy leads to a 1D finite element model with *ad-hoc* coefficients that implicitly include the generally non-constant description of the transverse dynamics. The possibility of locally tuning the modal expansion to match spatial heterogeneities represents one of the main strengths of the HiMod approach [10].

In this paper, we focus on the pointwise HiMod reduction strategy proposed in [11], where the modal tuning is performed on the finite element nodes. For this reason, the pointwise approach turns out to be the most flexible one among the available HiMod procedures [12], being suited to model both localized and widespread dynamics. In particular, with a view to practical applications, we extend the pointwise HiMod formulation to an unsteady setting by resorting to a discretization discontinuous in time. We generalize the cG(s)-dG(q) formulation in [13, 14, 15] to the HiMod setting, by defining a reduced solution that we denote by c[M(\mathbf{M})G(s)]-dG(q) approximation. Essentially, we replace the full model with a solution that is continuous in space and discontinuous in time. It is obtained via a Galerkin approximation that combines finite elements of degree s with the modal expansion identified by the index \mathbf{M} to discretize the space, and discontinuous piecewise polynomials of degree q for the time discretization.

The selection of the modal distribution as well as of the space-time discretization represents a crucial step of the HiMod reduction. To overcome this issue, we devise a procedure able to automatically predict the HiMod solution, for fixed values of s and q . By replicating the offline/online paradigm adopted in [16], we distinguish an offline phase, the computationally most expensive one, from an online phase which is computationally very cheap. The offline phase yields the so-called *HiMod lookup diagram*, i.e., a table

that sets the time partition and then, for each time interval, selects the corresponding 1D finite element mesh together with the associated modal distribution. The lookup diagram is the final outcome of an adaptive procedure based on an *a posteriori* analysis of the global (modeling plus space-time discretization) error. We rely upon a goal-oriented setting [17, 18, 19], so that the prediction of the $c[\mathbf{M}(\mathbf{M})\mathbf{G}(s)]\text{-dG}(q)$ model is driven by a physical quantity of reference.

The estimator for the global error consists of a modeling and of a discretization contribution, which are distinct [20, 16, 21, 10]. This represents a crucial property with a view to a global adaptation algorithm. In particular, the modeling estimator is a generalization of the goal-oriented hierarchical *a posteriori* error estimator derived in [10] to a time dependent setting, while including the temporal discontinuities of the $c[\mathbf{M}(\mathbf{M})\mathbf{G}(s)]\text{-dG}(q)$ scheme. The estimator for the discretization error, in turn, keeps separate the temporal from the spatial contribution [22, 23, 24, 25] and it is obtained by modifying the standard goal-oriented analysis to include the intrinsic dimensionally hybrid nature of a HiMod approximation [10].

The task of the online phase simply consists in computing the pointwise HiMod solution associated with the HiMod lookup diagram.

A first validation of the HiMod reduction procedure is also provided in this paper, by dealing with an experimental and modeling study of solute transport in porous media [26].

2 The full setting

We introduce the parabolic model we aim at reducing via an adaptive space-time model reduction procedure. A standard notation is adopted for the Sobolev spaces associated with the spatial independent variable only, as well as for the space of the functions bounded almost everywhere [27]. Concerning a space-time dependence, we introduce the spaces $L^2(0, T; W) = \{v : (0, T) \rightarrow W : \int_0^T \|v(t)\|_W^2 dt < +\infty\}$, $H^1(0, T; W) = \{v, \frac{\partial v}{\partial t} \in L^2(0, T; W)\}$, $C^0([0, T]; W) = \{v : [0, T] \rightarrow W \text{ continuous} : \forall t \in [0, T], \|v(t)\|_W < +\infty\}$, where W denotes a generic Hilbert space, with $\|\cdot\|_W$ the associated norm [28].

2.1 The problem

We select as model to be reduced the unsteady problem

$$\begin{cases} \frac{\partial u}{\partial t}(\mathbf{z}, t) + Lu(\mathbf{z}, t) = f(\mathbf{z}, t) & (\mathbf{z}, t) \in Q = \Omega \times I, \\ u(\mathbf{z}, t) = 0 & (\mathbf{z}, t) \in \partial Q_D = \Gamma_D \times I, \\ D\nabla u(\mathbf{z}, t) \cdot \mathbf{n} = g(\mathbf{z}, t) & (\mathbf{z}, t) \in \partial Q_N = \Gamma_N \times I, \\ u(\mathbf{z}, 0) = u_0(\mathbf{z}) & \mathbf{z} \in \Omega, \end{cases} \quad (1)$$

where $\Omega \subset \mathbb{R}^d$ ($d = 2, 3$) is the computational domain, Γ_D and Γ_N constitute a measurable non overlapping partition of $\partial\Omega$ such that $\partial\Omega = \Gamma_D \cup \Gamma_N$ and $\overset{\circ}{\Gamma}_D \cap \overset{\circ}{\Gamma}_N = \emptyset$, $I = (0, T)$ is the time window of interest, and L is a generic second-order elliptic operator with diffusive contribution given by $-\nabla \cdot (D\nabla u)$ so that $D\nabla u \cdot \mathbf{n} \equiv \partial_\nu u$ is the conormal derivative of u , \mathbf{n} being the unit outward normal vector to $\partial\Omega$. Concerning the data, we choose the source $f \in L^2(0, T; L^2(\Omega))$, the diffusivity tensor $D = [d_{ij}] \in [L^\infty(\Omega)]^{d \times d}$ such that the uniform ellipticity condition holds, the initial datum $u_0 \in L^2(\Omega)$, and the Neumann datum $g \in L^2(0, T; L^2(\Gamma_N))$. In the next section, further requirements are added on the computational domain as well as on the boundary conditions in view of the HiMod procedure.

The weak formulation associated with (1) is given by: find $u \in V = L^2(0, T; H_{\Gamma_D}^1(\Omega)) \cap H^1(0, T; (H_{\Gamma_D}^1(\Omega))')$, with $(H_{\Gamma_D}^1(\Omega))'$ the dual space of $H_{\Gamma_D}^1(\Omega)$, such that

$$\int_Q \frac{\partial u}{\partial t} v \, d\Omega \, dt + \int_I a(u, v) \, dt = \int_Q f v \, d\Omega \, dt + \int_{\partial Q_N} g v \, ds \, dt \quad \forall v \in V, \quad (2)$$

with $u(\mathbf{x}, 0) = u_0(\mathbf{x})$ and where $a(\cdot, \cdot) : H_{\Gamma_D}^1(\Omega) \times H_{\Gamma_D}^1(\Omega) \rightarrow \mathbb{R}$ is the bilinear form associated with operator L , here assumed continuous and coercive. Problem (2) represents the *full problem*, with u the full solution. The continuous embedding $V \hookrightarrow C^0([0, T]; L^2(\Omega))$ ensures the temporal continuity to the weak solution u in (2).

2.2 The computational domain

Problems suited to a HiMod reduction are usually defined on domains characterized by a prevalent dimension and the leading dynamics are aligned with such a dimension.

Thus, we assume Ω to coincide with the d -dimensional fiber bundle $\Omega = \bigcup_{x \in \Omega_{1D}} \{x\} \times \gamma_x$, where Ω_{1D} is the supporting 1D fiber described by the independent variable x and aligned with the dominant dynamics, while $\gamma_x \subset \mathbb{R}^{d-1}$ denotes the transverse fiber that is, in general, a function of x and parallel to the transverse dynamics. For the sake of simplicity, we assume $\Omega_{1D} \equiv]x_0, x_1[$ to be rectilinear and we refer to [29] for the more general case of a curved supporting fiber. We partition the boundary $\partial\Omega$ of Ω into three disjoint sets, $\Gamma_0 = \{x_0\} \times \gamma_{x_0}$, $\Gamma_1 = \{x_1\} \times \gamma_{x_1}$ and $\Gamma_* = \bigcup_{x \in \Omega_{1D}} \partial\gamma_x$, such that $\partial\Omega = \Gamma_0 \cup \Gamma_1 \cup \Gamma_*$ (see Remark 3.1 for further details).

Now, we map the domain Ω into a reference bundle $\widehat{\Omega}$, where the computations are easier, free from undetermined constants, and are carried out once and for all. To this aim, for any $x \in \Omega_{1D}$, we introduce the map $\psi_x : \gamma_x \rightarrow \widehat{\gamma}_{d-1}$ between the generic fiber γ_x and the reference fiber $\widehat{\gamma}_{d-1} \subset \mathbb{R}^{d-1}$. Maps ψ_x are instrumental to define the global map $\Psi : \Omega \rightarrow \widehat{\Omega}$, where $\widehat{\Omega} = \bigcup_{x \in \Omega_{1D}} \{x\} \times \widehat{\gamma}_{d-1}$ denotes the reference computational domain

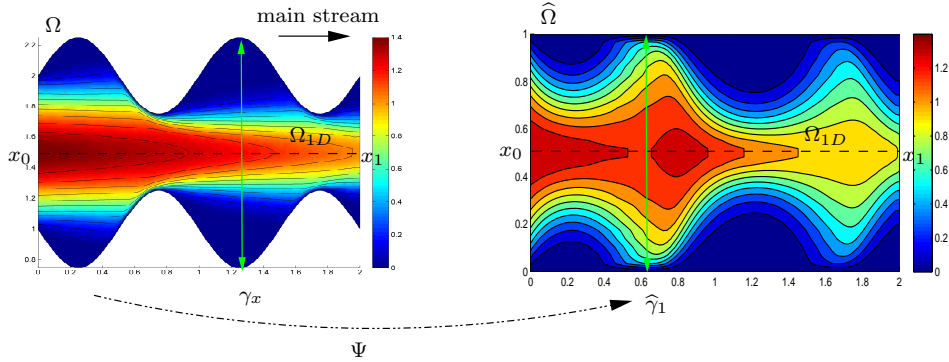


Figure 1: Map Ψ between a 2D sinusoidal domain Ω and the rectangular reference domain $\hat{\Omega}$.

(see Figure 1 for an example of map Ψ). Regularity assumptions are introduced on the maps ψ_x and Ψ . In particular, we assume ψ_x to be a C^1 -diffeomorphism, for all $x \in \Omega_{1D}$, and Ψ to be differentiable with respect to \mathbf{z} (essentially to exclude any kinks along Γ_*).

We also demand that the supporting fiber Ω_{1D} is preserved by map Ψ , so that the generic point $\mathbf{z} = (x, \mathbf{y}) \in \Omega$ is mapped into $\hat{\mathbf{z}} = \Psi(\mathbf{z}) = (\hat{x}, \hat{\mathbf{y}})$, with $\hat{x} \equiv x$ and $\hat{\mathbf{y}} = \psi_x(\mathbf{y})$. Finally, without reducing the generality, we assume Ω_{1D} to be the subset of Ω with $\mathbf{y} = \mathbf{0}$, i.e., Ω_{1D} exactly coincides with the centerline of Ω .

Remark 2.1. *In a 2D setting, we may always select ψ_x as a linear transformation, so that $\hat{\mathbf{y}} = \psi_x(\mathbf{y}) = \mathbf{y}/L(x)$, with $L(x) = \text{meas}(\gamma_x)$. In 3D a similar choice is possible only for specific configurations, for instance when Ω is a cylindrical domain. In this case $L(x)$ coincides with area of the diameter of the pipe along the centerline.*

3 HiMod reduction

The HiMod technique has been proposed in [8, 9] with the idea of exploiting the fiber structure demanded on Ω , or, likewise, the preferential dynamics in the phenomenon at hand. Currently, three versions of HiMod reduction have been investigated, from both a theoretical and a numerical viewpoint (see [12] for a survey on the different approaches). Independently of the selected technique, the idea is to manage in a different way the dependence of the solution on the leading and on the transverse dynamics. In particular, since HiMod aims at providing enriched 1D models to be associated with the dominant direction, only the dominant dynamic is discretized via a standard finite element scheme, while getting information on the transverse dynamics via a modal expansion.

In this section, we consider two of the available HiMod formulations.

3.1 Uniform HiMod reduction

The distinguishing feature of a uniform HiMod formulation is the adoption of a unique level of detail (i.e., the same number of modal functions) in modeling the transverse dynamics. For the sake of simplicity, we start from a steady setting. The function space associated with a uniform HiMod approach is

$$V_m = \left\{ v_m(x, \mathbf{y}) = \sum_{j=1}^m \tilde{v}_j(x) \varphi_j(\psi_x(\mathbf{y})), \text{ with } \tilde{v}_j \in V_{1D} \right\}, \quad (3)$$

where $m \in \mathbb{N}^+$ is a given integer, $V_{1D} \subseteq H^1(\Omega_{1D})$, and $\mathcal{B} = \{\varphi_j\}_{j \in \mathbb{N}^+}$ is a modal basis of functions in $H^1(\widehat{\gamma}_{d-1})$, orthonormal with respect to the $L^2(\widehat{\gamma}_{d-1})$ -scalar product. The boundary conditions assigned on Γ_0 and Γ_1 are taken into account by the space V_{1D} , while the boundary data on Γ_* are included in \mathcal{B} . Space V_m represents the hierarchy of models. We complete definition (3) by adding a conformity ($V_m \subset V$) and a spectral approximability ($\lim_{m \rightarrow +\infty} \inf_{v_m \in V_m} \|v - v_m\|_V = 0$, for any $v \in V$) hypothesis on V_m [8, 9].

With a view to unsteady problems, we introduce a time partition of the time window I into N subintervals $I_n = (t_{n-1}, t_n]$ of width $k_n = t_n - t_{n-1}$, for $n = 1, \dots, N$, with $k = \max_n k_n$, $t_0 \equiv 0$ and $t_N \equiv T$. This partition induces a subdivision of the cylinder Q into N space-time slabs $S_n = \Omega \times I_n$ with $n = 1, \dots, N$. Notice that partition $\{t_i\}_{i=0}^N$ is not necessarily uniform, to match the possible time heterogeneities of the problem at hand.

Now, we look for an approximate solution to (2) coinciding, on each space-time slab S_n , with a polynomial of degree at most q in time, with $q \in \mathbb{N}^+$, and with an element of V_m in space, i.e., a function of the reduced space

$$V_m^N = \left\{ v_m : (0, T] \rightarrow H_{\Gamma_D}^1(\Omega) : \forall n = 1, \dots, N \right. \\ \left. v_m(x, \mathbf{y}, t)|_{I_n} = \sum_{r=0}^q \sum_{j=1}^m t^r \tilde{v}_{j,r}^n(x) \varphi_{j,r}(\psi_x(\mathbf{y})), \text{ with } \tilde{v}_{j,r}^n \in V_{1D} \right\}. \quad (4)$$

The boundary conditions in (2) identifies V_{1D} with $H_{\gamma_D}^1(\Omega_{1D})$, where γ_D is a subset of $\{0, 1\}$ according to the definition of Γ_D , while functions $\varphi_{j,r}$ belong to the modal basis \mathcal{B} . Moreover, since $0 \notin I_1$, the value $v_m(x, \mathbf{y}, 0)$ has to be specified separately.

Remark 3.1. *The analysis below is completely general with respect to the boundary data. So far the robustness of the HiMod reduction has been verified when either homogeneous Dirichlet or homogeneous Neumann boundary conditions are assigned on Γ_0 , Γ_1 , Γ_* , or when non-homogeneous Dirichlet data are enforced on Γ_0 and Γ_1 . In general, the critical point is the*

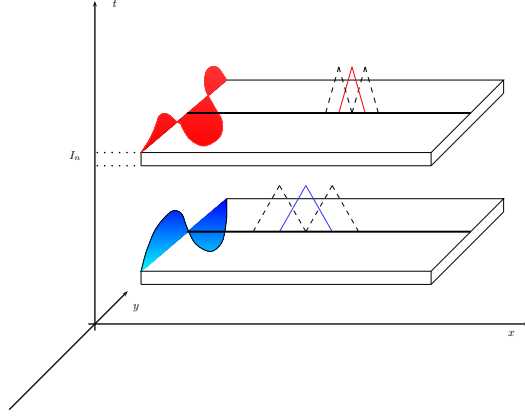


Figure 2: Example of modal distribution and finite element discretization associated with a slabwise uniform HiMod reduction.

identification of a basis \mathcal{B} matching Robin boundary conditions or non homogeneous data on Γ_ . A new strategy with respect to this issue is currently under investigation in [30].*

A priori functions in V_m^N may exhibit a discontinuity at each time level, with continuity from the left. As a consequence, a different number of modal functions can be selected on each time interval I_n (see Figure 2). This choice leads to replace in (4) the modal index m with the index $m_n \in \mathbb{N}^+$ with $n = 1, \dots, N$. In such a case we adopt the term *space-time slabwise uniform HiMod reduction* and we change the notation in (4) into $V_{\mathbf{m}}^N$, where $\mathbf{m} = [m_1, \dots, m_N]' \in [\mathbb{N}^+]^N$ is the vector that collects the number of modes used on each interval I_n , with $v_{\mathbf{m}}$ the generic function in $V_{\mathbf{m}}^N$.

The possible time discontinuity in $V_{\mathbf{m}}^N$ leads us to distinguish between the values $v_{\mathbf{m}}^{n,+} = \lim_{t \rightarrow 0^+} v_{\mathbf{m}}(x, \mathbf{y}, t_n + t)$ and $v_{\mathbf{m}}^{n,-} = \lim_{t \rightarrow 0^+} v_{\mathbf{m}}(x, \mathbf{y}, t_n - t)$, and to define the temporal jump $[v_{\mathbf{m}}]^n = v_{\mathbf{m}}^{n,+} - v_{\mathbf{m}}^{n,-}$ at the generic time t_n , for $n = 0, \dots, N - 1$. Notice that this jump is identically equal to zero for functions in V . This remark allows us to provide a weak formulation for problem (1) equivalent to (2): find $u \in V$ such that

$$\mathcal{A}_{\text{cGdG}}(u, v) = \mathcal{F}_{\text{cGdG}}(v) \quad \forall v \in V, \quad (5)$$

where, for any $w, \zeta \in V$,

$$\begin{aligned} \mathcal{A}_{\text{cGdG}}(w, \zeta) &= \sum_{n=1}^N \left\{ \int_{S_n} \frac{\partial w}{\partial t} \zeta \, d\Omega \, dt + \int_{I_n} a(w, \zeta) \, dt \right\} \\ &+ \sum_{i=1}^{N-1} \int_{\Omega} [w]^i \zeta^{i,+} \, d\Omega + \int_{\Omega} w^{0,+} \zeta^{0,+} \, d\Omega \end{aligned} \quad (6)$$

$$\mathcal{F}_{\text{cGdG}}(\zeta) = \int_{\Omega} w^{0,-} \zeta^{0,+} \, d\Omega + \sum_{n=1}^N \left\{ \int_{S_n} f \zeta \, d\Omega \, dt + \int_{\partial Q_N^n} g \zeta \, ds \, dt \right\} \quad (7)$$

with $u^{0,+} = u^{0,-} = u_0(x, \mathbf{y})$ and $\partial Q_N^n = \Gamma_N \times I_n$ for $n = 1, \dots, N$.

The space-time *slabwise uniform* HiMod formulation can thus be stated: find $u_{\mathbf{m}} \in V_{\mathbf{m}}^N$ such that, for any $v_{\mathbf{m}} \in V_{\mathbf{m}}^N$,

$$\mathcal{A}_{\text{cGdG}}(u_{\mathbf{m}}, v_{\mathbf{m}}) = \mathcal{F}_{\text{cGdG}}(v_{\mathbf{m}}). \quad (8)$$

The jump terms in (6) provide now an actual contribution, and we distinguish between the HiMod approximation $u_{\mathbf{m}}^{0,-} \in V_{\mathbf{m}}^N|_{I_1}$ of the initial datum u_0 and $u_{\mathbf{m}}^{0,+}$ that is unknown.

The conformity and the spectral approximability hypotheses are now added slabwise to guarantee the well-posedness of formulation (8). Indeed, due to the discontinuity in time, we can only expect that $V_{\mathbf{m}}^N|_{S_n} \subset V|_{S_n}$, while $V_{\mathbf{m}}^N \not\subset V$.

Concerning the spatial discretization, following [8, 9], we consider a finite element discretization of the function dependence on x by introducing a subdivision, not necessarily uniform, of the supporting fiber into subintervals. The time discontinuity admits the adoption of different partitions on each space-time slab (see Figure 2). In particular, we denote by $\mathcal{T}_{h_n} = \{K_l^n\}_{l=1}^{\mathcal{M}_n}$ the spatial partition associated with S_n for $n = 1, \dots, N$, with $K_l^n = (x_{l-1}^n, x_l^n)$ the generic subinterval of width $h_l^n = x_l^n - x_{l-1}^n$ for $l = 1, \dots, \mathcal{M}_n$, with $h_n = \max_l h_l^n$ and $x_0^n \equiv x_0$, $x_{\mathcal{M}_n}^n \equiv x_1$. Then, we furnish each S_n with the space $X_{h_n}^{1D,s}$ of the conforming finite elements of degree s associated with \mathcal{T}_{h_n} , and with $\dim(X_{h_n}^{1D,s}) = N_{h_n} < +\infty$. A standard density hypothesis in V_{1D} is advanced on each finite element space.

Thus, the discrete counterpart of formulation (8) is: find $u_{\mathbf{m}}^h \in V_{\mathbf{m},h}^N$ such that, for any $v_{\mathbf{m}}^h \in V_{\mathbf{m},h}^N$,

$$\mathcal{A}_{\text{cGdG}}(u_{\mathbf{m}}^h, v_{\mathbf{m}}^h) = \mathcal{F}_{\text{cGdG}}(v_{\mathbf{m}}^h), \quad (9)$$

where

$$\begin{aligned} V_{\mathbf{m},h}^N &= \left\{ v_{\mathbf{m}}^h : (0, T] \rightarrow H_{\Gamma_D}^1(\Omega) : \forall n = 1, \dots, N \right. \\ &\left. v_{\mathbf{m}}^h(x, \mathbf{y}, t)|_{I_n} = \sum_{r=0}^q \sum_{j=1}^{m_n} t^r \tilde{v}_{j,r}^{n,h}(x) \varphi_{j,r}(\psi_x(\mathbf{y})), \text{ with } \tilde{v}_{j,r}^{n,h} \in X_{h_n}^{1D,s} \cap V_{1D} \right\}, \end{aligned} \quad (10)$$

$u_{\mathbf{m}}^{h,0,-} \in V_{\mathbf{m},h}^N|_{I_1}$ is a discrete HiMod approximation of u_0 , and $u_{\mathbf{m}}^{h,0,+}$ is an unknown¹. It follows $V_{\mathbf{m},h}^N \subset V_{\mathbf{m}}^N$, i.e., also the discrete HiMod space $V_{\mathbf{m},h}^N$ consists of functions continuous in space but discontinuous in time. Notice that, although $V_{\mathbf{m},h}^N \not\subset V$, in (9) we can extend definitions (6) and (7) to $V_{\mathbf{m},h}^N$ taking advantage of the slabwise splitting.

By generalizing the notation used in [13, 14, 15] to denote finite elements that are continuous in space and discontinuous in time, we refer to $V_{\mathbf{m},h}^N$ as to the HiMod $c[M(\mathbf{m})G(s)]\text{-dG}(q)$ space (and, analogously, to (9) as to the $c[M(\mathbf{m})G(s)]\text{-dG}(q)$ HiMod formulation). We mean that, on each S_n , the full solution is replaced by a reduced solution continuous in space and discontinuous in time, obtained via a Galerkin approximation based on finite elements of degree s combined with the modal expansion associated with the multi-index \mathbf{m} to discretize the space, and piecewise polynomials of degree q for the time discretization.

The finite element discretization along Ω_{1D} allows us to further expand the Fourier coefficient $\tilde{v}_{j,r}^{n,h}$ in (10) in terms of the finite element basis $\{\vartheta_l\}_{l=1}^{N_{h_n}}$ associated with space $X_{h_n}^{1D,s}$, so that any function $v_{\mathbf{m}}^h \in V_{\mathbf{m},h}^N$ can be represented on the generic time interval I_n as

$$v_{\mathbf{m}}^h(x, \mathbf{y}, t)|_{I_n} = \sum_{r=0}^q \sum_{j=1}^{m_n} \sum_{l=1}^{N_{h_n}} t^r \tilde{v}_{j,r,l}^{n,h} \vartheta_l(x) \varphi_{j,r}(\psi_x(\mathbf{y})) \quad (11)$$

with $n = 1, \dots, N$. The coefficients $\tilde{u}_{j,r,l}^{n,h}$ of $u_{\mathbf{m}}^h$ become the actual unknowns of the $c[M(\mathbf{m})G(s)]\text{-dG}(q)$ HiMod formulation (9).

3.2 Pointwise HiMod reduction

A fixed number of modal functions on the whole Ω may become too restrictive in the presence of spatial heterogeneities. This justifies the formalization of HiMod strategies alternative to the uniform approach, where a different number of modes is adopted in different subdomains of Ω (via a piecewise HiMod reduction, [9, 10]), rather than in correspondence with each finite element node (via a pointwise HiMod reduction, [11]). We focus on the last approach. The numerical verification in [11] identifies the pointwise method as the best-performing one in the presence of either widespread or localized transverse dynamics.

The idea exploited in a pointwise HiMod expansion consists in rewriting (11) by emphasizing the sum on the finite element nodes, i.e., as

$$v_{\mathbf{m}}^h(x, \mathbf{y}, t)|_{I_n} = \sum_{l=1}^{N_{h_n}} \vartheta_l(x) \left[\sum_{r=0}^q \sum_{j=1}^{m_n} t^r \tilde{v}_{j,r,l}^{n,h} \varphi_{j,r}(\psi_x(\mathbf{y})) \right],$$

¹To simplify notations, with the super-index h we understand both the space and time discretizations

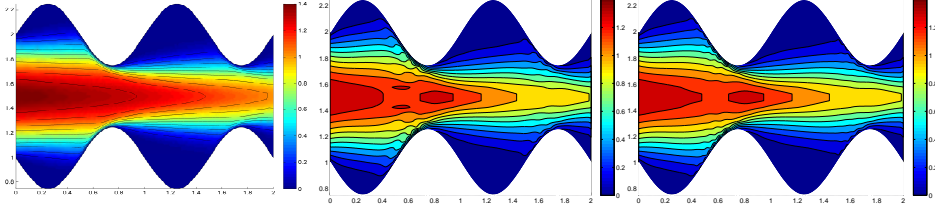


Figure 3: Wavy channel test case: full solution (left); uniform HiMod solution for $m = 11$ (center) and $m = 21$ (right).

and then in making the modal index m_n dependent on the nodal index l . Space $V_{\mathbf{m},h}^N$ is thus replaced by the new space

$$V_{\mathbf{M},h}^N = \left\{ v_{\mathbf{M}}^h : (0, T] \rightarrow H_{\Gamma_D}^1(\Omega) : \forall n = 1, \dots, N \right. \quad (12)$$

$$\left. v_{\mathbf{M}}^h(x, \mathbf{y}, t)|_{I_n} = v_{\mathbf{M}_n}^h(x, \mathbf{y}, t) = \sum_{l=1}^{N_{h_n}} \vartheta_l(x) \left[\sum_{r=0}^q \sum_{j=1}^{m_{n,l}} t^r \tilde{v}_{j,r,l}^{n,h} \varphi_{j,r}(\psi_x(\mathbf{y})) \right] \right\},$$

where $\mathbf{M}_n = [m_{n,1}, \dots, m_{n,N_{h_n}}]' \in [\mathbb{N}^+]^{N_{h_n}}$ is the modal nodewise vector collecting the number of modes used at each finite element node of the slab S_n for $n = 1, \dots, N$, whereas \mathbf{M} is just the subindex used to denote a pointwise HiMod approximation. The nodewise tuning of the number of modes leads to an algebraic system sharing the same sparsity pattern as for the uniform case, but with a smaller dimension [11].

The formulation related to space $V_{\mathbf{M},h}^N$ coincides with a space-time *pointwise* HiMod reduction and will be denoted by $c[\mathbf{M}(\mathbf{M})\mathbf{G}(s)]\text{-dG}(q)$ form. It reads exactly as (9), simply by replacing space $V_{\mathbf{m},h}^N$ with $V_{\mathbf{M},h}^N$. Notice that, since definition (12) strictly depends on the finite element discretization, there does not exist a weak counterpart of the pointwise formulation.

3.2.1 Uniform versus pointwise HiMod reduction: an example

We compare the uniform and the pointwise HiMod approaches on the steady test case 4 in [9], where the transport of oxygen in a wavy channel, representing a Bellhouse oxygenator for extra-corporeal circulation [31], is modeled. This problem is characterized by a widespread dynamics, that is suited to be reduced via both these techniques.

Figure 3, left shows the full solution u computed on an unstructured uniform mesh of about 15000 elements and via 2D affine finite elements. The irregular shape of the domain strongly affects the main stream of the flow on the whole domain as highlighted by the bent contour lines.

As far the HiMod reduction, we discretize the dependence of u on x via affine finite elements after introducing a partition of uniform step $h = 0.1$

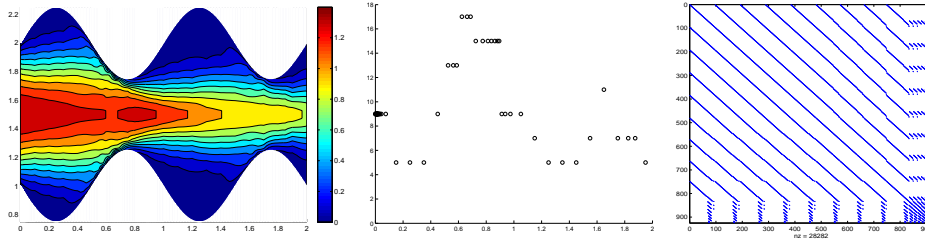


Figure 4: Wavy channel test case: nodewise HiMod solution (left) with corresponding modal distribution (center) and sparsity pattern (right).

on Ω_{1D} . The transverse dynamics are described with a basis \mathcal{B} of sinusoidal functions. To evaluate the integrals of the modal functions, we resort to Gaussian quadrature formulas based on four quadrature nodes per wavelength, at least. No stabilization scheme is used.

We first apply the uniform HiMod approach by resorting to 11 and 21 modal functions. As shown in [9], at least 11 modes are required to obtain a sufficiently reliable HiMod approximation. Figure 3, center and right shows the contour plots of the discrete HiMod solutions u_{11}^h and u_{21}^h , respectively. The two reduced solutions are very similar. In particular, the innermost contour lines associated with u_{21}^h are more accurate.

As second assessment, we build the pointwise HiMod approximation $u_{\mathbf{M}}^h$ associated with the modal distribution \mathbf{M} in Figure 4, center. As shown in Figure 4, left it is fully comparable with the uniform approximation u_{21}^h , despite the overall smaller number of modes (the maximum number of modes equal to 17 is used only in correspondence with three finite element nodes). This leads to a considerable saving in terms of computational cost. Indeed, instead of the 176400 (420×420) system associated with u_{21}^h , we solve a system of dimension 28282, whose sparsity pattern is shown in Figure 4, right.

In accordance with [11], results in Figures 3-4 show the improved modeling capabilities of the pointwise HiMod method vs the uniform approach, for a fixed computational effort. Clearly, the main issue related to a pointwise formulation is the choice of the nodewise modal distribution. This corroborates the need for an automatic modal selection.

4 Adaptive HiMod reduction

In this section we deal with both the offline and the online phases of the adaptive HiMod procedure. At this stage, we use a uniform and sufficiently fine discretization $\{(x_l^n, t_n)_{l=1}^{M_n}\}_{n=1}^N$ on $\Omega_{1D} \times I$.

Due to its significant impact on practical applications, we consider a goal-oriented framework (see, e.g., [17, 18, 19]), so that the reduced model

predicted by the offline phase fits a goal functional that represents a physical quantity of interest (e.g., mean or pointwise values, fluxes across sections or regions, the energy of the system at hand, the vorticity of a turbulent flow). We denote by J the selected functional and we assume it is linear. We aim at approximating, within a prescribed tolerance TOL , the value $J(u)$, with u solution to the full problem (2), via $J(u_{\mathbf{M}}^h)$, where $u_{\mathbf{M}}^h$ is the reduced solution associated with the HiMod diagram yielded by the offline phase. The computation of the value $J(u_{\mathbf{M}}^h)$ represents the goal of the online phase.

4.1 The *a posteriori* modeling error analysis

We generalize the error analysis in [10] to an unsteady setting, thus deriving the theoretical tool used to set up the HiMod lookup diagram, i.e., a table that furnishes the number of modes to be switched on at each finite element node x_l^n and at each time t_n of the space-time partition (see Figure 7, left for an example). The *a posteriori* analysis is carried out starting from the slabwise uniform HiMod formulation (8), while the pointwise approximation $u_{\mathbf{M}}^h$ will constitute the output of the adaptive procedure in the next section.

According to a goal-oriented approach, we introduce the dual problem associated with (8) given by: find $z_{\mathbf{m}} \in V_{\mathbf{m}}^N$ such that, for any $v_{\mathbf{m}} \in V_{\mathbf{m}}^N$,

$$\mathcal{A}_{\text{cGdG}}(v_{\mathbf{m}}, z_{\mathbf{m}}) = J_{\text{cGdG}}(v_{\mathbf{m}}), \quad (13)$$

where, for any $\zeta \in V \cup V_{\mathbf{m}}^N$,

$$J_{\text{cGdG}}(\zeta) = \int_{\Omega} z_{\mathbf{m}}^{N,+} \zeta^{N,-} d\Omega + \sum_{n=1}^N \int_{\tilde{S}_n} \tilde{j} \zeta d\Omega dt, \quad (14)$$

where \tilde{j} is the density function associated with the goal functional J . Notice that, since $V_{\mathbf{m}}^N \not\subset V$, J has to be defined on $V \cup V_{\mathbf{m}}^N$ and analogously for J_{cGdG} . A null final condition, $z_{\mathbf{m}}^{N,+} = 0$, allows to get rid of the first integral in (14), whereas boundary contributions may characterize the definition of J_{cGdG} when functional J involves a control on the boundary. The assignment of boundary conditions to the dual problem is a crucial issue that is usually tackled via the Lagrange identity.

Remark 4.1. *The bilinear form $\mathcal{A}_{\text{cGdG}}(w, \zeta)$ in (6) can be alternatively rewritten integrating by parts the time derivative, and after recombining the jump terms. We have*

$$\sum_{n=1}^N \left\{ - \int_{\tilde{S}_n} \frac{\partial \zeta}{\partial t} w d\Omega dt + \int_{I_n} a(w, \zeta) dt \right\} - \sum_{i=1}^{N-1} \int_{\Omega} [\zeta]^i w_m^{i,-} d\Omega + \int_{\Omega} \zeta^{N,-} w^{N,-} d\Omega,$$

for any $w, \zeta \in V \cup V_{\mathbf{m}}^N$. This form better fits the dual setting due to the reverse time scale.

To derive the *a posteriori* modeling error estimator, we introduce also the enriched primal and dual slabwise uniform HiMod problems,

$$\text{find } u_{\mathbf{m}}^+ \in V_{\mathbf{m}^+}^N \quad \text{s.t.} \quad \mathcal{A}_{\text{cGdG}}(u_{\mathbf{m}^+}, v_{\mathbf{m}^+}) = \mathcal{F}_{\text{cGdG}}(v_{\mathbf{m}^+}) \quad \forall v_{\mathbf{m}^+} \in V_{\mathbf{m}^+}^N, \quad (15)$$

$$\text{find } z_{\mathbf{m}}^+ \in V_{\mathbf{m}^+}^N \quad \text{s.t.} \quad \mathcal{A}_{\text{cGdG}}(v_{\mathbf{m}^+}, z_{\mathbf{m}^+}) = J_{\text{cGdG}}(v_{\mathbf{m}^+}) \quad \forall v_{\mathbf{m}^+} \in V_{\mathbf{m}^+}^N, \quad (16)$$

with $\mathbf{m}^+ > \mathbf{m}$ (i.e., $m_i^+ > m_i$ for $i = 1, \dots, N$). The inclusion $V_{\mathbf{m}}^N \subset V_{\mathbf{m}^+}^N$ guarantees the orthogonality relations

$$\mathcal{A}_{\text{cGdG}}(u_{\mathbf{m}^+} - u_{\mathbf{m}}, v_{\mathbf{m}}) = 0, \quad \mathcal{A}_{\text{cGdG}}(v_{\mathbf{m}}, z_{\mathbf{m}^+} - z_{\mathbf{m}}) = 0 \quad \forall v_{\mathbf{m}} \in V_{\mathbf{m}}^N.$$

The analysis derived in [10] can be applied to the slabwise HiMod formulation with due changes, to state the following

Proposition 1. *Let $e_{\mathbf{m}} = u - u_{\mathbf{m}} \in V \cup V_{\mathbf{m}}^N$ and $e_{\mathbf{m}^+} = u - u_{\mathbf{m}^+} \in V \cup V_{\mathbf{m}^+}^N$ be the modeling error associated with the reduced formulation (8) and (15), respectively for $\mathbf{m}, \mathbf{m}^+ \in [\mathbb{N}^+]^N$ and with $\mathbf{m}^+ > \mathbf{m}$. Let us assume that both the final dual data $z_{\mathbf{m}}^{N,+}$ and $z_{\mathbf{m}^+}^{N,+}$ are identically equal to zero. Then, if there exists a positive constant $\sigma_{\mathbf{m}} < 1$ and a modal multi-index $\mathbf{M}_0 \in [\mathbb{N}^+]^N$ such that, for $\mathbf{m}^+ > \mathbf{m} \geq \mathbf{M}_0$,*

$$|J(e_{\mathbf{m}^+})| \leq \sigma_{\mathbf{m}} |J(e_{\mathbf{m}})|, \quad (17)$$

the following two-sided inequality holds

$$\frac{|J(\delta u_{\mathbf{m}\mathbf{m}^+})|}{1 + \sigma_{\mathbf{m}}} \leq |J(e_{\mathbf{m}})| \leq \frac{|J(\delta u_{\mathbf{m}\mathbf{m}^+})|}{1 - \sigma_{\mathbf{m}}}, \quad (18)$$

with $\delta u_{\mathbf{m}\mathbf{m}^+} = u_{\mathbf{m}^+} - u_{\mathbf{m}}$.

The proof of estimate (18) exactly coincides with the one of Proposition 2 in [10]. In particular, the requirement on the dual final data identifies J_{cGdG} with functional J . Provided the saturation assumption (17) to hold, result (18) identifies the modeling error estimator $\eta_{\mathbf{m}\mathbf{m}^+}$ for the error $J(e_{\mathbf{m}})$ with the value $|J(\delta u_{\mathbf{m}\mathbf{m}^+})|$, while guaranteeing the efficiency and the reliability of $\eta_{\mathbf{m}\mathbf{m}^+}$ via the lower and upper bound in (18), respectively. Following [10], to evaluate estimator $\eta_{\mathbf{m}\mathbf{m}^+}$, we can adopt three equivalent formulas, given by

$$\eta_{\mathbf{m}\mathbf{m}^+} = \mathcal{A}_{\text{cGdG}}(\delta u_{\mathbf{m}\mathbf{m}^+}, \delta z_{\mathbf{m}\mathbf{m}^+}) = \rho_p(u_{\mathbf{m}})(z_{\mathbf{m}^+}) = \rho_d(z_{\mathbf{m}})(u_{\mathbf{m}^+}) \quad (19)$$

with $\delta z_{\mathbf{m}\mathbf{m}^+} = z_{\mathbf{m}^+} - z_{\mathbf{m}}$, and where $\rho_p(u_{\mathbf{m}})(\cdot) = \mathcal{F}_{\text{cGdG}}(\cdot) - \mathcal{A}_{\text{cGdG}}(u_{\mathbf{m}}, \cdot)$, and $\rho_d(z_{\mathbf{m}})(\cdot) = J_{\text{cGdG}}(\cdot) - \mathcal{A}_{\text{cGdG}}(\cdot, z_{\mathbf{m}})$ denote the weak primal and dual residuals associated with the HiMod formulations (8) and (13), respectively. Moreover, to make computable $\eta_{\mathbf{m}\mathbf{m}^+}$, we replace the reduced primal and dual solutions with corresponding discrete approximations.

Estimator $\eta_{\mathbf{m}\mathbf{m}^+}$ exhibits the structure typical of a hierarchical error estimator, yet in a goal-oriented framework. We refer to [10] for more computational remarks and for some considerations on requirement (17) that represents a generalization of the standard saturation assumption [32, 33, 34] to a goal-oriented setting.

4.2 Construction of the HiMod lookup diagram

Estimator $\eta_{\mathbf{mm}^+}$ is now used to select the pointwise HiMod approximation $u_{\mathbf{M}}^h$ for problem (2) able to guarantee the desired accuracy TOL on the functional error $J(u - u_{\mathbf{M}}^h)$.

To start the adaptive procedure, we assign two initial (and possibly small) values to the uniform modal indices m and m^+ . Then, the adopted algorithm consists of the following five stages:

- S1) we compute the discrete uniform reduced primal and dual solutions, $u_m^h, u_{m^+}^h, z_m, z_{m^+}^h$, on the whole space-time cylinder Q ;
- S2) we evaluate the modeling estimator $\eta_{mm^+}^n = \eta_{mm^+}|_{S_n}$ localized to each space-time slab S_n ;
- S3) we apply the adaptive procedure outlined in Figure 5 to predict the nodewise modal distribution \mathbf{M}_n associated with each slab S_n , i.e., the HiMod lookup diagram (see below for all the details);
- S4) we compute the discrete pointwise reduced primal and dual solutions, $u_{\mathbf{M}}^h, u_{\mathbf{M}^+}^h, z_{\mathbf{M}}, z_{\mathbf{M}^+}^h$, associated with the HiMod diagram yielded at stage S3);
- S5) we evaluate the modeling error estimator $\eta_{\mathbf{MM}^+}$ on the pointwise solutions identified at stage S4). Then, if the global tolerance is met, i.e., $\eta_{\mathbf{MM}^+} \leq \text{TOL}$, the procedure stops, providing the HiMod lookup diagram in S3) as final outcome. Vice versa, if $\eta_{\mathbf{MM}^+} > \text{TOL}$, we come back to S2).

Before detailing the adaptive procedure at stage S3), some remarks are in order.

The computational effort associated with stage S1) takes advantage of the time discontinuity of the $c[\mathbf{M}(\mathbf{M})\mathbf{G}(s)]\text{-dG}(q)$ scheme. More sophisticated approaches such as checkpointing [35] may be clearly adopted to further reduce the computational costs. The modeling estimator can obviously be evaluated in correspondence with any HiMod approximation (uniform as in S2), slabwise uniform as in (19), pointwise as in S5)). Indeed, via the first definition in (19), it suffices to evaluate the bilinear form (6) on the HiMod solutions at hand, by exploiting the slabwise definition of $\mathcal{A}_{\text{cGdG}}(\cdot, \cdot)$. Concerning the localization of the estimator to slab S_n at stage S2), by exploiting again the first definition in (19), we have

$$\begin{aligned} \eta_{mm^+}^n &= \mathcal{A}_{\text{cGdG}}(\delta u_{mm^+}, \delta z_{mm^+})|_{S_n} = \\ & \int_{S_n} \frac{\partial \delta u_{mm^+}}{\partial t} \delta z_{mm^+} d\Omega dt + \int_{I_n} a(\delta u_{mm^+}, \delta z_{mm^+}) dt + \int_{\Omega} [\delta u_{mm^+}]^{n-1} \delta z_{mm^+}^{n-1,+} d\Omega. \end{aligned} \quad (20)$$

Finally, the HiMod pointwise approximations $u_{\mathbf{M}}^h$, $z_{\mathbf{M}}^h$ and $u_{\mathbf{M}^+}^h$, $z_{\mathbf{M}^+}^h$ at stage S4) are the solutions to problems (5), (13) and (15), (16) settled in the space $V_{\mathbf{M},h}^N$ and $V_{\mathbf{M}^+,h}^N$, respectively. In particular, we assume that $V_{\mathbf{M},h}^N$ and $V_{\mathbf{M}^+,h}^N$ share the same spatial partitions \mathcal{T}_{h_n} for $n = 1, \dots, N$, so that \mathbf{M}^+ identifies reduced solutions with a pointwise larger number of modes with respect to $u_{\mathbf{M}}^h$ and $z_{\mathbf{M}}^h$.

Let us focus now on the adaptive procedure devised to commute the local evaluations of η_{mm^+} into the lookup diagram predicted at stage S3). To this aim, we consider the generic space-time slab S_n and we focus on the case of linear finite elements. We proceed in the following way:

- S3.1) we assign a number of modes equal to m to each node and to each subinterval of partition \mathcal{T}_{h_n} ;
- S3.2) we evaluate the estimator $\eta_{mm^+}^{n,l} = \eta_{mm^+}^n|_{K_l^n}$ localized to each interval K_l^n of \mathcal{T}_{h_n} , for $l = 1, \dots, \mathcal{M}_n$, simply by exploiting the additive property of the integrals involved in the definition of η_{mm^+} ;
- S3.3) we invoke an equidistribution criterion of the modeling error on the slab S_n as well as on the subintervals K_l^n . If $\eta_{mm^+}^{n,l} > \text{TOL} \delta_{1\text{M}}/(N\mathcal{M}_n)$, we increase by one the modal index associated with K_l^n (model refinement); if $\eta_{mm^+}^{n,l} < \text{TOL} \delta_{2\text{M}}/(N\mathcal{M}_n)$, we decrease by one such an index (model coarsening); otherwise, we preserve the current modal index;
- S3.4) we update the number of modes associated with each finite element node by assigning to the generic node x_l^n , for $l = 1, \dots, \mathcal{M}_n - 1$, a number of modes equal to $m_{n,l} = \min(m_{K_l^n}, m_{K_{l+1}^n})$, with $m_{K_l^n}$ the number of modes assigned on the interval K_l^n . In particular, to avoid an abrupt variation of modes on consecutive nodes, the actual value $m_{n,l}^*$ associated with x_l^n coincides with $\max(0.5 m_{n,l-1} + 0.5 m_{n,l+1} - 3, m_{n,l})$. The endpoints of Ω_{1D} are updated separately as $m_{n,0} = m_{K_1^n}$ and $m_{n,\mathcal{M}_n} = m_{K_{\mathcal{M}_n}^n}$ if Dirichlet boundary conditions are not imposed on Γ_0 and on Γ_1 , respectively. The assignment of the modal indices $m_{n,l}$ predicts the modal multi-index $\mathbf{M}_n = [m_{n,1}, \dots, m_{n,N_{h_n}}]'$ for the slab S_n .

The procedure in S3) is exemplified in Figure 5 for a partition \mathcal{T}_{h_n} of Ω_{1D} consisting only of three subintervals K_l^n ($l = 1, 2, 3$) and when linear finite elements are considered.

Of course, steps S3.1)-S3.4) are applied to the enriched modal index m^+ as well, with a view to the evaluation of the modeling error estimator at stage S5).

The adaptive modal algorithm includes both model refinement and coarsening. A minimum number of modes constrains the modal coarsening, while

a maximum number of adaptive iterations is fixed to avoid too restrictive demands on TOL. The tuning parameters δ_{1M} and δ_{2M} at stage S3.3) make the adaptive algorithm more robust, while increasing the corresponding computational efficiency. We set $\delta_{1M} = 0.5$, $\delta_{2M} = 1.5$.

Finally, the modal update at step S3.4) plays a crucial role in making effective the final outcome of the adaptive procedure since it explains how to build a pointwise approximation u_M^h starting from any HiMod lookup diagram.

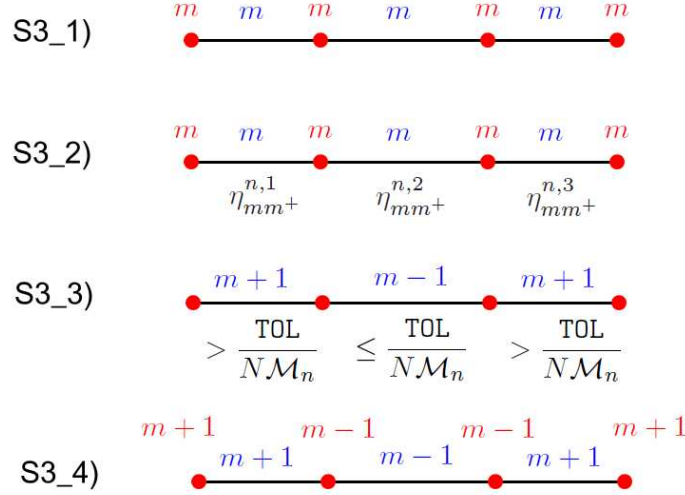


Figure 5: Example of the modal adaptive procedure at stage S3).

4.3 Numerical verification of the HiMod lookup diagram

The numerical verification of the paper is carried out in a 2D setting. Moreover, to select the discrete HiMod space, we choose $q = 0$ and $s = 1$, i.e., we use linear finite elements to discretize the leading dynamics and functions piecewise constant in time. It can be checked that the adopted time discretization is equivalent to a modified backward Euler scheme [14].

We validate the reliability of the adaptive HiMod reduction procedure by approximating problem (1) on the rectangular domain $\Omega = (0, 3) \times (0, 1)$ for $t \in I = (0, 1)$, and by choosing $Lu = -\Delta u + \mathbf{c} \cdot \nabla u$ with $\mathbf{c} = [10, 0]^T$. Besides the directionality induced by the advective field, we introduce a local heterogeneity via the source term $f \equiv 10\chi_{\mathcal{D}}$, with $\chi_{\mathcal{D}}$ the characteristic function associated with the elliptic region $\mathcal{D} = \{(x, y) : (x - 1.5)^2 + 4(y - 0.25)^2 \leq 0.01\}$. Concerning the boundary conditions, homogeneous Dirichlet data are assigned on $\partial\Omega \setminus \Gamma_N$, with $\Gamma_N = \{(3, y) : 0 \leq y \leq 1\}$, where a homogeneous Neumann datum is enforced. Finally, a null initial datum u_0 is chosen. In Figure 6, left we show at five different times, the contour plots of

the full solution u approximated via a standard 2D cG(1)-dG(0) scheme on a uniform unstructured mesh of 10252 triangles. As expected, the convective field acts on the purely diffusive phenomenon by horizontally bending the contour lines.

From a modeling viewpoint, we are simulating the process of convection and diffusion of a certain pollutant emitted, for instance, by a chimney localized at \mathcal{D} , in the presence of a moderate horizontal wind. In this context, the full solution u represents the pollutant concentration in the domain Ω at a certain time $t \in I$

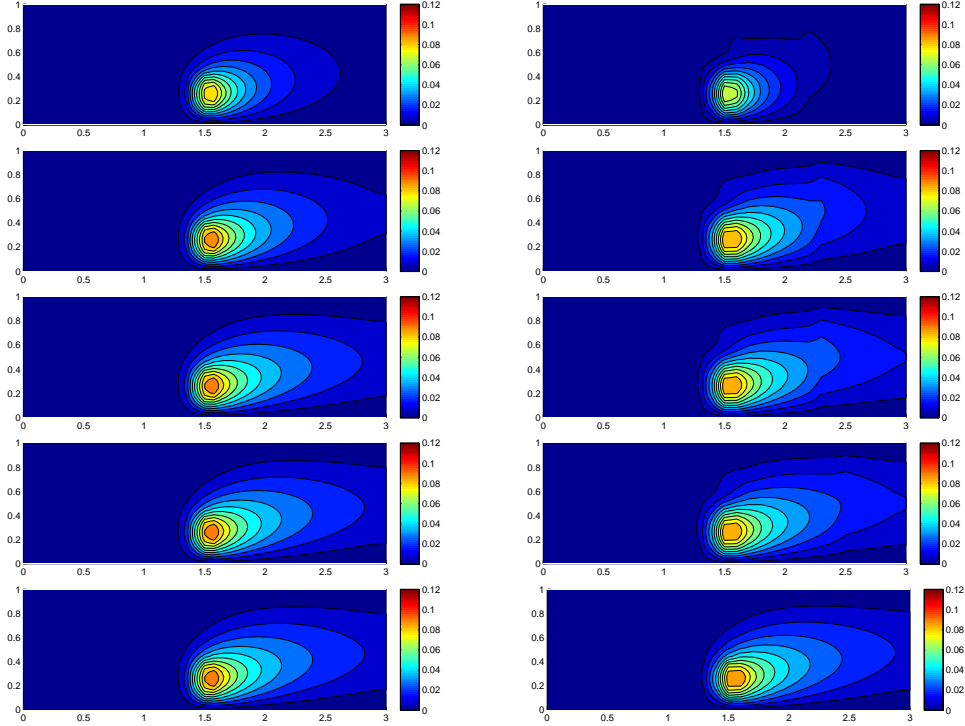


Figure 6: Convection-diffusion of a pollutant, control of $J_{\text{mean},T}$, modal adaptation: full solution (left) and HiMod approximation $u_{\mathbf{M}}^h$ (right), for $t = 0.1, 0.2, 0.5, 0.8, 1$ (top-bottom).

The offline phase is set up to control the mean value of the full solution on the whole Ω but only at the final time $T = 1$. This is equivalent to select the goal functional J as $J_{\text{mean},T}(\zeta) = [\text{meas}(\Omega)]^{-1} \int_{\Omega} \zeta(x, y, 1) d\Omega$. The choice of a localized (in time) functional is a challenging choice with a view to the modeling adaptive procedure. The dual problem is characterized by the differential operator $L^*z = -\Delta z - \mathbf{c} \cdot \nabla z$, with source term given by the density function $\tilde{j}(x, y, t) = [\text{meas}(\Omega)]^{-1} \delta_T$ associated with $J_{\text{mean},T}$, where δ_T denotes the Dirac distribution associated with the final time. On Γ_N a homogeneous Robin boundary condition is imposed, while a homogeneous

Dirichlet datum is assigned on $\partial\Omega \setminus \Gamma_N$. A null final value $z_{\mathbf{m}}^{N,+}$ is selected.

Both the primal and dual problems involved in the evaluation of the error estimator $\eta_{\mathbf{mm}^+}$ are computed by discretizing the supporting fiber $(0, 3) \times \{0.5\}$ via a uniform partition of size $h = 0.15$ and the time window with a constant step $k = 0.1$. The modal basis \mathcal{B} consists of sinusoidal functions.

Finally, the modeling tolerance TOL is set to 10^{-2} , while the uniform modal indices m and m^+ are set to 1 and 3, respectively.

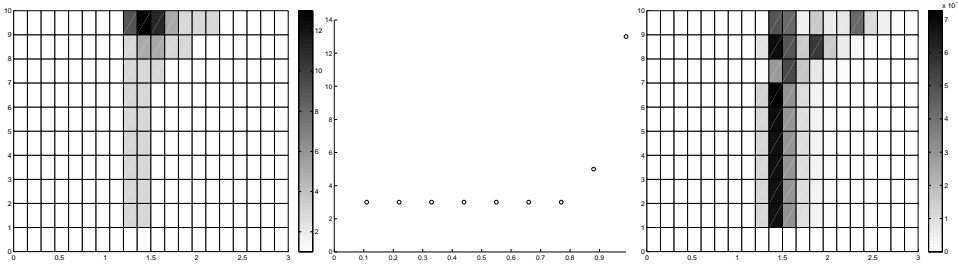


Figure 7: Convection-diffusion of a pollutant, control of $J_{\text{mean},T}$, modal adaptation: HiMod lookup diagram (left); modal distribution at $x=1.5$ as a function of time (center); space-time distribution of $\eta_{\mathbf{MM}^+}$ (right).

The adaptive algorithm converges after 21 iterations. Figure 7, left depicts the output of the offline phase, i.e., the HiMod lookup diagram that predicts how many modes (colormap) have to be used at each finite element node (horizontal side) and for each time (vertical side) to guarantee that $|J_{\text{mean},T}(u) - J_{\text{mean},T}(u_{\mathbf{M}}^h)| < \text{TOL}$.

The diagram coincides with the space-time rectangle $\Omega_{1D} \times I$, where Ω_{1D} and I exhibit the corresponding partition of uniform size h and k , respectively. A certain number of modal functions is associated with each cell $K_l^n \times k$ for $l = 1, \dots, \mathcal{M}_n$ and $n = 1, \dots, N$. Thus, by resorting to the procedure in Figure 5, S3.4) it is possible to build the HiMod pointwise approximation $u_{\mathbf{M}_n}^h$ for each $n = 1, \dots, N$, i.e., the reduced solution $u_{\mathbf{M}}^h$.

The HiMod diagram in Figure 7, left shows that few modes are demanded on the whole space-time domain, except for the two last time intervals, where a larger number of modes is switched on in correspondence with the localized source and the downstream region. More quantitative information are provided by the plot in Figure 7, center of the number of modes associated with node $x = 1.5$ as a function of time. Only 3 modes are used on the whole time interval except for the subintervals I_{N-1} and I_N when 5 and 13 sine functions are required, respectively. The modal distribution predicted by the lookup diagram is completely coherent with a goal-oriented approach. Since we are interested in the mean value of the solution only at the final time, it is reasonable to expect a reliable approximation of the full solution

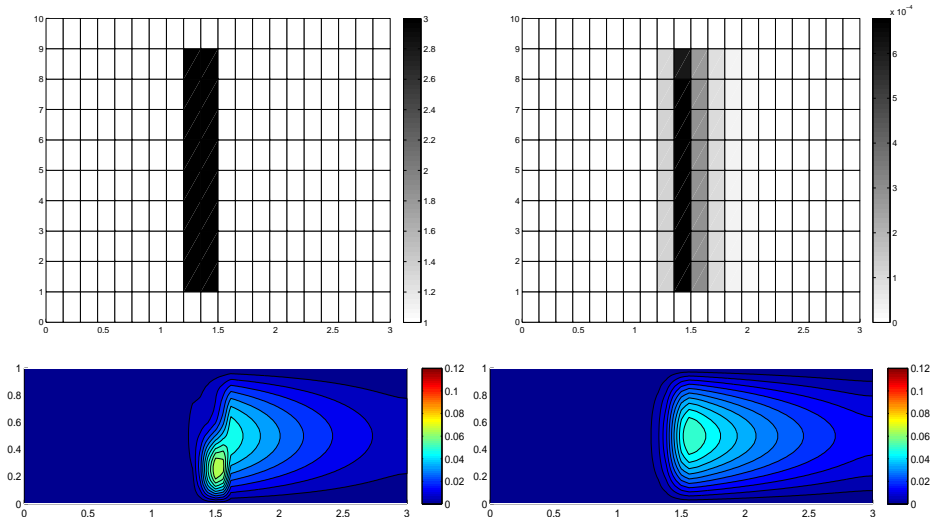


Figure 8: Convection-diffusion of a pollutant, control of $J_{\text{mean},T}^{\text{left}}$, modal adaptation: HiMod lookup diagram (top-left); space-time distribution of η_{MM^+} (top-right); HiMod approximation u_{M}^h (bottom) at $t = 0.2$ (left) and $t = T$ (right).

only in correspondence with the last time intervals. This trend is confirmed by the online phase that provides a pointwise HiMod approximation which is more similar to the full one in Figure 6, left during the last times of the simulation (see Figure 6, right).

In Figure 7, right we show the value of η_{MM^+} on the same space-time structure of the HiMod diagram. The boxes associated with the largest values of the estimator identify a pattern similar to the one in Figure 7, left.

To check the sensitivity of the adaptive HiMod procedure with respect to the selected goal functional, we run the offline phase by preserving all the input parameters, with $J = J_{\text{mean},T}^{\text{left}}(\zeta) = [\text{meas}(\Omega^{\text{left}})]^{-1} \int_{\Omega^{\text{left}}} \zeta(x, y, 1) d\Omega^{\text{left}}$, with $\Omega^{\text{left}} = (0, 1.2) \times (0, 1)$. We deal now with a functional localized both in time and space. The adaptive procedure stops after only three iterations by providing the HiMod lookup diagram in Figure 8, top-left. A single mode is adopted on the whole time window in Ω^{left} where the solution is flat. The modeling error estimator identifies the portion of the domain around \mathcal{D} as the most problematic one, to be refined in terms of modal expansion (see Figure 8, top-right). As highlighted in the HiMod diagram, to ensure tolerance TOL, three sinusoidal functions are used in the two consecutive subintervals just before $x = 1.5$ for almost the whole time window. On the contrary, during the last time interval, a single mode is active on the whole Ω . The $c[\text{M}(\mathbf{M})\text{G}(1)]\text{-dG}(0)$ HiMod approximation at two different times is shown in Figure 8, bottom. In agreement with a goal-oriented approach,

the reduced solution is far from the full one in Figure 6, left especially at T . The mean value is controlled in an area where the full solution is extremely smooth so that a single mode suffices to describe a so regular trend.

5 Combined HiMod reduction and space-time adaptation

Goal of this section is to enrich the information provided by the HiMod lookup diagram to predict also the space-time partition on Ω_{1D} and I . This leads us to remove any assumption on the finite element discretization as well as on the time partition $\{I_n\}$. In practice, we expect to replace the diagram in Figure 7, left with a new diagram characterized by a non uniform horizontal (spatial) and vertical (temporal) spacing.

5.1 The *a posteriori* estimator for the global error

With a view to a global adaptation, following, e.g., [20, 16, 21, 10], we derive an *a posteriori* estimator for the global error $\mathcal{E}_{\mathbf{m}}^h = e_{\mathbf{m}} + e_{\mathbf{m}}^h$, where the contributions of the modeling ($e_{\mathbf{m}} = u - u_{\mathbf{m}}$) and of the discretization ($e_{\mathbf{m}}^h = u_{\mathbf{m}} - u_{\mathbf{m}}^h$) errors remain distinct. In particular, since we are interested also in an adaptive selection of the space and time step size, we expect that the estimator for the discretization error consists of a spatial contribution separate from the temporal one [22, 23, 24, 25].

As for the adaptive HiMod reduction, we carry out the *a posteriori* analysis in a slabwise uniform HiMod setting. The pointwise HiMod approximation predicted by the offline phase will be generated during the online phase.

The following statement plays a crucial role in the definition of the global error estimator.

Proposition 2. *We assume that saturation assumption (17) holds, and we choose $z_{\mathbf{m}^+}^{N,+} = z_{\mathbf{m}^+}^{N,+} = 0$. Then, for any $\mathbf{m}, \mathbf{m}^+ \in [\mathbb{N}^+]^N$, with $\mathbf{m}^+ > \mathbf{m} \geq \mathbf{M}_0$ and \mathbf{M}_0 defined as in Proposition 1, it turns out that*

$$|J(\mathcal{E}_{\mathbf{m}}^h)| \leq \frac{1}{1 - \sigma_{\mathbf{m}}} \left(|J(\delta u_{\mathbf{m}\mathbf{m}^+})| + |J(e_{\mathbf{m}}^h)| \right). \quad (21)$$

Moreover, if there exists a constant λ with $0 < \lambda < 1$, such that

$$|J(e_{\mathbf{m}}^h)| \leq \lambda |J(e_{\mathbf{m}})|, \quad (22)$$

it additionally holds that

$$|J(\mathcal{E}_{\mathbf{m}}^h)| \geq \frac{1 - \lambda}{3 + \sigma_{\mathbf{m}} - \lambda} \left(|J(\delta u_{\mathbf{m}\mathbf{m}^+})| + |J(e_{\mathbf{m}}^h)| \right). \quad (23)$$

Proof. Estimates (21) and (23) follow from Proposition 3 and 4 in [10], respectively. \square

Starting from Proposition 2, we adopt the quantity

$$\eta_{\mathbf{m}\mathbf{m}^+}^h = |J(\delta u_{\mathbf{m}\mathbf{m}^+})| + |J(e_{\mathbf{m}}^h)| \quad (24)$$

as the *a posteriori* error estimator for the global error $\mathcal{E}_{\mathbf{m}}^h$. As a consequence, inequalities (21) and (23) state the reliability and the efficiency of such an estimator. The first term of $\eta_{\mathbf{m}\mathbf{m}^+}^h$ exactly coincides with the modeling error estimator in (19), while the second contribution takes into account the error associated with both the spatial and the temporal discretizations. The main effort of this section will be to explicitly estimate this term, with the additional requirement of distinguishing the space from the time contribution. As in [10], we have to properly modify the standard goal-oriented analysis to tackle the intrinsic dimensionally hybrid nature of a HiMod reduced formulation.

Concerning hypothesis (22), it essentially coincides with a sufficient grid resolution requirement since establishing a ratio between the modeling and the discretization errors.

With a view to estimate $|J(e_{\mathbf{m}}^h)|$, we preliminarily prove the following Galerkin orthogonality property for the discretization error $e_{\mathbf{m}}^h$.

Lemma 3. *For any $v_{\mathbf{m}}^h \in V_{\mathbf{m},h}^N$, the following relation holds*

$$\sum_{n=1}^N \left\{ \int_{S_n} \frac{\partial e_{\mathbf{m}}^h}{\partial t} v_{\mathbf{m}}^h d\Omega dt + \int_{I_n} a(e_{\mathbf{m}}^h, v_{\mathbf{m}}^h) dt + \int_{\Omega} [e_{\mathbf{m}}^h]^{n-1} v_{\mathbf{m}}^{h,n-1,+} d\Omega \right\} = 0. \quad (25)$$

Proof. We consider the HiMod formulation (8) and the corresponding discrete counterpart (9). The time discontinuity characterizing spaces $V_{\mathbf{m}}^N$ and $V_{\mathbf{m},h}^N$ allows us to select the values of $v_{\mathbf{m}}$ and $v_{\mathbf{m}}^h$ independently on each I_n for $n = 1, \dots, N$. Thus, we pick both $v_{\mathbf{m}}$ and $v_{\mathbf{m}}^h$ to vanish outside I_n so that formulations (8) and (9) reduce to a unique equation on I_n : find $u_{\mathbf{m}} \in V_{\mathbf{m}}^N|_{S_n}$ such that, for any $v_{\mathbf{m}} \in V_{\mathbf{m}}^N|_{S_n}$,

$$\mathcal{A}_{\text{cGdG}}(u_{\mathbf{m}}, v_{\mathbf{m}})|_{S_n} = \mathcal{F}_{\text{cGdG}}(v_{\mathbf{m}})|_{S_n}, \quad (26)$$

and, likewise, find $u_{\mathbf{m}}^h \in V_{\mathbf{m},h}^N|_{S_n}$ such that, for any $v_{\mathbf{m}}^h \in V_{\mathbf{m},h}^N|_{S_n}$,

$$\mathcal{A}_{\text{cGdG}}(u_{\mathbf{m}}^h, v_{\mathbf{m}}^h)|_{S_n} = \mathcal{F}_{\text{cGdG}}(v_{\mathbf{m}}^h)|_{S_n}, \quad (27)$$

with $\mathcal{A}_{\text{cGdG}}(w, \zeta)|_{S_n}$ defined as in (20) and

$$\mathcal{F}_{\text{cGdG}}(\zeta)|_{S_n} = \int_{S_n} f\zeta d\Omega dt + \int_{\partial Q_N^n} g\zeta ds dt,$$

with $w, \zeta \in V \cup V_{\mathbf{m}}^h$. Now, since $V_{\mathbf{m},h}^N|_{S_n} \subset V_{\mathbf{m}}^N|_{S_n}$, we subtract (27) from (26) after identifying $v_{\mathbf{m}}$ with $v_{\mathbf{m}}^h$, to get the orthogonality relation

$$\mathcal{A}_{\text{cGdG}}(e_{\mathbf{m}}^h, v_{\mathbf{m}}^h)|_{S_n} = 0, \quad (28)$$

for any $n = 1, \dots, N$. Identity (28) can now be generalized to an arbitrary function $v_{\mathbf{m}}^h \in V_{\mathbf{m},h}^N$ by suitably summing through the slabs. This yields identity (25). \square

Some notations are now instrumental. Let R_l^n be the region of Ω defined by $\bigcup_{x \in K_l^n} \{x\} \times \gamma_x$, with K_l^n the generic subinterval of \mathcal{T}_{h_n} , while we denote the interface between R_τ^n and $R_{\tau+1}^n$ by ζ_τ^n , for $\tau = 1, \dots, \mathcal{M}_n - 1$ and $n = 1, \dots, N$, and with $\zeta_0^n \equiv \Gamma_0$ and $\zeta_{\mathcal{M}_n}^n \equiv \Gamma_1$. Finally, $S_{R_l^n} = R_l^n \times I_n$ denotes the space-time prism associated with R_l^n , while $L_{R_l^n} = \partial R_l^n \times I_n$ identifies the corresponding lateral surface.

We introduce now the spatial and temporal local residuals. For a fixed time interval I_n and for any R_l^n , we consider the internal residual

$$r_{R_l^n} = \left(f - \frac{\partial u_{\mathbf{m}}^h}{\partial t} - L_l^n u_{\mathbf{m}}^h \right) \Big|_{S_{R_l^n}} \quad (29)$$

and the boundary residual

$$j_{R_l^n} = \begin{cases} 0 & \text{on } (\partial R_l^n \cap \Gamma_D) \times I_n \\ 2(g - \partial_\nu u_{\mathbf{m}}^h)|_{S_{R_l^n}} & \text{on } (\partial R_l^n \cap \Gamma_N) \times I_n \\ -[\partial_\nu u_{\mathbf{m}}^h] & \text{on } (\partial R_l^n \cap \mathcal{E}_h^n) \times I_n \end{cases}$$

associated with the discrete HiMod solution $u_{\mathbf{m}}^h$, with $l = 1, \dots, \mathcal{M}_n$ and $n = 1, \dots, N$, where L_l^n is the restriction of the elliptic operator L in (1) to the prism $S_{R_l^n}$ and $[\partial_\nu u_{\mathbf{m}}^h]$ is the jump of the conormal derivative of $u_{\mathbf{m}}^h$ across an edge of the skeleton $\mathcal{E}_h^n = \{\zeta_\tau^n\}_{\tau=1}^{\mathcal{M}_n-1}$. We consider now the temporal residual associated with $u_{\mathbf{m}}^h$ and with the time level t_n

$$\mathcal{J}_n = [-u_{\mathbf{m}}^h]^n = (-u_{\mathbf{m}}^{h,n,+} + u_{\mathbf{m}}^{h,n,-}), \quad (30)$$

together with the initial error

$$e_{\mathbf{m}}^{h,0,-} = u_{\mathbf{m}}^{0,-} - u_{\mathbf{m}}^{h,0,-}. \quad (31)$$

Finally, we introduce a spatial and a temporal operator. In particular, we consider the time projection operator $T_n : V_{\mathbf{m}}^N|_{S_n} \rightarrow H_{\Gamma_D}^1(\Omega)$, for $n = 1, \dots, N$, such that

$$T_n v = \frac{1}{k_n} \int_{I_n} v dt \quad \forall v \in V_{\mathbf{m}}^N|_{S_n},$$

and the one-dimensional Clément quasi-interpolant $\mathcal{I}^1 : L^2(\Omega_{1D}) \rightarrow \mathbb{R}$ [36]. By definition, the projection error $v - T_n v$ is orthogonal to any function c constant in time, so that

$$\int_{I_n} (v - T_n v) c \, dt = 0 \quad \forall v \in V_{\mathbf{m}}^N|_{S_n}, \quad (32)$$

whereas the estimate

$$\|v - T_n v\|_{L^2(I_n)} \leq k_n \left\| \frac{\partial v}{\partial t} \right\|_{L^2(I_n)} \quad \forall v \in V_{\mathbf{m}}^N|_{S_n} \quad (33)$$

can be proved [15]. Notice that no constant is involved in this result. Concerning the Clément quasi-interpolant, the estimates

$$\|v - \mathcal{I}^1(v)\|_{L^2(K)} \leq \mathcal{C}_1 h_K |v|_{H^1(\tilde{K})} \quad (34)$$

$$\|v - \mathcal{I}^1(v)\|_{L^2(\partial K)} \leq \mathcal{C}_2 h_K^{1/2} \|v\|_{H^1(\tilde{K})} \quad (35)$$

hold, for any $v \in H^1(\Omega_{1D})$, where K denotes a generic interval of Ω_{1D} , \tilde{K} is the associated patch of elements, and with \mathcal{C}_1 and \mathcal{C}_2 constants depending on the relative size of the elements constituting \tilde{K} [36].

We are now ready to prove the following result:

Proposition 4. *Let $\Omega \subset \mathbb{R}^2$. Let us assume that the approximation $u_{\mathbf{m}}^{h,0,-}$ of the initial datum coincide with the L^2 -projection $\mathcal{P}_{I_1}(u_{\mathbf{m}}^{0,-})$ of $u_{\mathbf{m}}^{0,-}$ onto the space $V_{\mathbf{m},h}^N|_{I_1}$. Moreover, we choose $z_{\mathbf{m}}^{N,+} = 0$. Then, the following estimate for the functional error $|J(e_{\mathbf{m}}^h)|$ holds*

$$|J(e_{\mathbf{m}}^h)| \leq \mathcal{C} \sum_{n=1}^N \sum_{l=1}^{\mathcal{M}_n} \left[\rho_{R_l^n}^S(u_{\mathbf{m}}^h) \omega_{R_l^n}^S(z_{\mathbf{m}} - z_{\mathbf{m}}^h) + \sum_{i=1}^2 \rho_{R_l^n}^{T_i}(u_{\mathbf{m}}^h) \omega_{R_l^n}^{T_i}(z_{\mathbf{m}} - z_{\mathbf{m}}^h) \right], \quad (36)$$

with \mathcal{C} a constant depending on the interpolation constants in (34)-(35), on q and on $\max_n m_n$, where the residuals are defined by

$$\begin{aligned} \rho_{R_l^n}^S(u_{\mathbf{m}}^h) &= h_l^n \|\bar{r}_{R_l^n}\|_{L^2(S_{R_l^n})} + \frac{1}{2} (h_l^n)^{\frac{1}{2}} \|\bar{j}_{R_l^n}\|_{L^2(L_{R_l^n})}, \\ &+ \frac{h_l^n}{k_n^{\frac{1}{2}}} \left(\|\mathcal{J}_{n-1}\|_{L^2(R_l^n)} + \|e_{\mathbf{m}}^{h,0,-}\|_{L^2(R_l^n)} \delta_{1,n} \right), \\ \rho_{R_l^n}^{T_1}(u_{\mathbf{m}}^h) &= k_n \|r_{R_l^n} - \bar{r}_{R_l^n}\|_{L^2(S_{R_l^n})} + k_n^{\frac{1}{2}} \left(\|\mathcal{J}_{n-1}\|_{L^2(R_l^n)} + \|e_{\mathbf{m}}^{h,0,-}\|_{L^2(R_l^n)} \delta_{1,n} \right), \\ \rho_{R_l^n}^{T_2}(u_{\mathbf{m}}^h) &= \frac{k_n}{2} \|j_{R_l^n} - \bar{j}_{R_l^n}\|_{L^2(L_{R_l^n})}, \end{aligned}$$

with $\bar{r}_{R_l^n} = T_n r_{R_l^n}$, $\bar{j}_{R_l^n} = T_n j_{R_l^n}$, h_l^n and k_n the length of the generic subinterval K_l^n and I_n , respectively for $l = 1, \dots, \mathcal{M}_n$ and $n = 1, \dots, N$, and with

$\delta_{1,n}$ the Kronecker symbol associated with the first slab S_1 , while the weights are given by

$$\begin{aligned}\omega_{R_l^n}^S(z_{\mathbf{m}} - z_{\mathbf{m}}^h) &= \left(\max_{x \in K_l^n} L(x) \right)^{\frac{1}{2}} \sum_{r=0}^q \sum_{j=1}^{m_n} \|\tilde{z}_{j,r}^n - \tilde{z}_{j,r}^{n,h}\|_{H^1(\tilde{K}_l^n)} \|t^r\|_{L^2(I_n)} \\ \omega_{R_l^n}^{T_1}(z_{\mathbf{m}} - z_{\mathbf{m}}^h) &= \left\| \frac{\partial(z_{\mathbf{m}} - z_{\mathbf{m}}^h)}{\partial t} \right\|_{L^2(S_{R_l^n})}, \quad \omega_{R_l^n}^{T_2}(z_{\mathbf{m}} - z_{\mathbf{m}}^h) = \left\| \frac{\partial(z_{\mathbf{m}} - z_{\mathbf{m}}^h)}{\partial t} \right\|_{L^2(L_{R_l^n})},\end{aligned}$$

with

$$\tilde{K}_l^n = \begin{cases} K_1^n \cup K_2^n, & \text{for } l = 1, \\ K_{l-1}^n \cup K_l^n \cup K_{l+1}^n & \text{for } l = 2, \dots, \mathcal{M}_n - 1 \\ K_{\mathcal{M}_n-1}^n \cup K_{\mathcal{M}_n}^n & \text{for } l = \mathcal{M}_n, \end{cases} \quad (37)$$

the patch associated with the subinterval K_l^n , $L(x) = \text{meas}(\gamma_x)$, $\tilde{z}_{j,r}^n$ and $\tilde{z}_{j,r}^{n,h}$ the modal coefficients associated with the dual solution $z_{\mathbf{m}}$ and with the corresponding discretization $z_{\mathbf{m}}^h$, respectively.

Proof. We start from the dual problem (13) by choosing $v_{\mathbf{m}} = e_{\mathbf{m}}^h$ and we apply the orthogonality relation (25). It follows that, for any $v_{\mathbf{m}}^h \in V_{\mathbf{m},h}^N$,

$$\begin{aligned}|J(e_{\mathbf{m}}^h)| &= |\mathcal{A}_{\text{cGdG}}(e_{\mathbf{m}}^h, z_{\mathbf{m}})| \\ &= \left| \sum_{n=1}^N \left\{ \int_{S_n} \frac{\partial e_{\mathbf{m}}^h}{\partial t} (z_{\mathbf{m}} - v_{\mathbf{m}}^h) d\Omega dt + \int_{I_n} a(e_{\mathbf{m}}^h, z_{\mathbf{m}} - v_{\mathbf{m}}^h) dt \right. \right. \\ &\quad \left. \left. - \int_{\Omega} [e_{\mathbf{m}}^h]^{n-1} v_{\mathbf{m}}^{h,n-1,+} d\Omega \right\} + \sum_{i=1}^{N-1} \int_{\Omega} [e_{\mathbf{m}}^h]^i z_{\mathbf{m}}^{i,+} d\Omega + \int_{\Omega} e_{\mathbf{m}}^{h,0,+} z_{\mathbf{m}}^{0,+} d\Omega \right|.\end{aligned}$$

The identification of $J_{\text{cGdG}}(e_{\mathbf{m}}^h)$ with $J(e_{\mathbf{m}}^h)$ follows from the requirement on the dual final datum. We add and subtract the value $\int_{\Omega} e_{\mathbf{m}}^{h,0,-} (z_{\mathbf{m}} - v_{\mathbf{m}}^h)^{0,+} d\Omega$, by exploiting in (31) the choice $u_{\mathbf{m}}^{h,0,-} = \mathcal{P}_{I_1}(u_{\mathbf{m}}^{0,-})$ for the primal initial datum. A manipulation of the jump contributions combined with the definition of projection operator yields

$$\begin{aligned}|J(e_{\mathbf{m}}^h)| &= \left| \sum_{n=1}^N \left\{ \int_{S_n} \frac{\partial e_{\mathbf{m}}^h}{\partial t} (z_{\mathbf{m}} - v_{\mathbf{m}}^h) d\Omega dt + \int_{I_n} a(e_{\mathbf{m}}^h, z_{\mathbf{m}} - v_{\mathbf{m}}^h) dt \right. \right. \\ &\quad \left. \left. + \int_{\Omega} [e_{\mathbf{m}}^h]^{n-1} (z_{\mathbf{m}} - v_{\mathbf{m}}^h)^{n-1,+} d\Omega \right\} + \int_{\Omega} e_{\mathbf{m}}^{h,0,-} (z_{\mathbf{m}} - v_{\mathbf{m}}^h)^{0,+} d\Omega \right|.\end{aligned}$$

After exploiting relation (26) with $v_{\mathbf{m}} = z_{\mathbf{m}} - v_{\mathbf{m}}^h$, we integrate by parts on

the regions R_l^n :

$$\begin{aligned}
|J(e_{\mathbf{m}}^h)| &= \left| \sum_{n=1}^N \sum_{l=1}^{\mathcal{M}_n} \left\{ \int_{I_n} \left[\int_{R_l^n} \left(f - \frac{\partial u_{\mathbf{m}}^h}{\partial t} - L_l^n u_{\mathbf{m}}^h \right) (z_{\mathbf{m}} - v_{\mathbf{m}}^h) dR_l^n \right. \right. \\
&+ \left. \int_{\partial R_l^n \cap \Gamma_N} g(z_{\mathbf{m}} - v_{\mathbf{m}}^h) ds - \int_{\partial R_l^n} \partial_\nu u_{\mathbf{m}}^h (z_{\mathbf{m}} - v_{\mathbf{m}}^h) ds \right] dt \\
&+ \left. \int_{R_l^n} [-u_{\mathbf{m}}^h]^{n-1} (z_{\mathbf{m}} - v_{\mathbf{m}}^h)^{n-1,+} dR_l^n \right\} + \sum_{\tilde{l}=1}^{M_1} \int_{R_{\tilde{l}}^1} e_{\mathbf{m}}^{h,0,-} (z_{\mathbf{m}} - v_{\mathbf{m}}^h)^{0,+} dR_{\tilde{l}}^1 \Big|.
\end{aligned}$$

Thanks to definitions (29)-(30), we have

$$\begin{aligned}
|J(e_{\mathbf{m}}^h)| &\leq \sum_{n=1}^N \sum_{l=1}^{\mathcal{M}_n} \left\{ \underbrace{\left| \int_{S_{R_l^n}} r_{R_l^n} (z_{\mathbf{m}} - v_{\mathbf{m}}^h) dR_l^n dt \right|}_{\text{(I)}} \right. \\
&+ \underbrace{\frac{1}{2} \left| \int_{L_{R_l^n}} j_{R_l^n} (z_{\mathbf{m}} - v_{\mathbf{m}}^h) ds dt \right|}_{\text{(II)}} + \underbrace{\left| \int_{R_l^n} \mathcal{J}_{n-1} (z_{\mathbf{m}} - v_{\mathbf{m}}^h)^{n-1,+} dR_l^n \right|}_{\text{(III)}} \Big\} \\
&+ \sum_{\tilde{l}=1}^{M_1} \underbrace{\left| \int_{R_{\tilde{l}}^1} e_{\mathbf{m}}^{h,0,-} (z_{\mathbf{m}} - v_{\mathbf{m}}^h)^{0,+} dR_{\tilde{l}}^1 \right|}_{\text{(IV)}}. \tag{38}
\end{aligned}$$

We consider separately the four terms (I)-(IV). In particular, we choose $v_{\mathbf{m}}^h$ coinciding with $z_{\mathbf{m}}^h + T_n(\mathcal{I}^1(z_{\mathbf{m}} - z_{\mathbf{m}}^h))$, with $z_{\mathbf{m}}^h$ the discrete HiMod approximation of the dual solution. In particular, the Clément operator involves only the x -dependent modal coefficients since it is one-dimensional. Notice that, since we estimate slabwise the terms (I)-(IV), all the functions in $V_{\mathbf{m}}^N$ and $V_{\mathbf{m},h}^N$ have to be meant restricted to I_n , for each $n = 1, \dots, N$. Function $v_{\mathbf{m}}^h$ is extended to zero outside I_n when considered as a function of $V_{\mathbf{m},h}^N$.

To exploit the projection and the interpolation estimates in (33)-(35), we consider the following splitting

$$z_{\mathbf{m}} - v_{\mathbf{m}}^h = [(z_{\mathbf{m}} - z_{\mathbf{m}}^h) - T_n(z_{\mathbf{m}} - z_{\mathbf{m}}^h) + T_n(z_{\mathbf{m}} - z_{\mathbf{m}}^h) - T_n(\mathcal{I}^1(z_{\mathbf{m}} - z_{\mathbf{m}}^h))]. \tag{39}$$

Let us focus on term (I). Using the splitting above, the definition of the averaged residual $\bar{r}_{R_l^n}$ and of the projection operation T_n , and by combining

results (32)-(33) with the Cauchy-Schwarz inequality, we obtain

$$\begin{aligned}
(\text{I}) &= \left| \int_{S_{R_l^n}} (r_{R_l^n} - \bar{r}_{R_l^n}) [z_{\mathbf{m}} - z_{\mathbf{m}}^h - T_n(z_{\mathbf{m}} - z_{\mathbf{m}}^h)] dR_l^n dt \right. \\
&\quad \left. + \int_{R_l^n} \left[T_n(z_{\mathbf{m}} - z_{\mathbf{m}}^h - \mathcal{I}^1(z_{\mathbf{m}} - z_{\mathbf{m}}^h)) \int_{I_n} r_{R_l^n} dt \right] dR_l^n \right| \\
&\leq \int_{R_l^n} \|r_{R_l^n} - \bar{r}_{R_l^n}\|_{L^2(I_n)} \|z_{\mathbf{m}} - z_{\mathbf{m}}^h - T_n(z_{\mathbf{m}} - z_{\mathbf{m}}^h)\|_{L^2(I_n)} dR_l^n \\
&\quad + \left| \int_{S_{R_l^n}} \bar{r}_{R_l^n} (z_{\mathbf{m}} - z_{\mathbf{m}}^h - \mathcal{I}^1(z_{\mathbf{m}} - z_{\mathbf{m}}^h)) dR_l^n dt \right| \\
&\leq k_n \|r_{R_l^n} - \bar{r}_{R_l^n}\|_{L^2(S_{R_l^n})} \left\| \frac{\partial(z_{\mathbf{m}} - z_{\mathbf{m}}^h)}{\partial t} \right\|_{L^2(S_{R_l^n})} \\
&\quad + \|\bar{r}_{R_l^n}\|_{L^2(S_{R_l^n})} \|(z_{\mathbf{m}} - z_{\mathbf{m}}^h - \mathcal{I}^1(z_{\mathbf{m}} - z_{\mathbf{m}}^h))\|_{L^2(S_{R_l^n})}.
\end{aligned}$$

We now consider separately the norm associated with the interpolation error. Let $w_{\mathbf{m}}$ be a generic element in $V_{\mathbf{m}}^N$. By exploiting the modal expansion for $w_{\mathbf{m}}$ and the orthonormality of the modal basis, together with interpolation estimate (34), we obtain

$$\begin{aligned}
\|w_{\mathbf{m}} - \mathcal{I}^1(w_{\mathbf{m}})\|_{L^2(S_{R_l^n})}^2 &= \int_{S_{R_l^n}} \left\{ \sum_{r=0}^q \sum_{j=1}^{m_n} t^r \varphi_{j,r}(\psi_x(y)) [\tilde{w}_{j,r}^n - \mathcal{I}^1(\tilde{w}_{j,r}^n)](x) \right\}^2 dR_l^n dt \\
&= \sum_{r=0}^q \sum_{j=1}^{m_n} \int_{I_n} t^{2r} \int_{K_l^n} \left[\int_{\hat{\gamma}_1} \varphi_{j,r}^2(\hat{y}) |\mathcal{D}^{-1}(x, \psi_x^{-1}(\hat{y}))| d\hat{y} \right] [\tilde{w}_{j,r}^n(x) - \mathcal{I}^1(\tilde{w}_{j,r}^n)(x)]^2 dK_l^n dt \\
&= \sum_{r=0}^q \sum_{j=1}^{m_n} \int_{I_n} t^{2r} \max_{x \in K_l^n} L(x) \|\tilde{w}_{j,r}^n - \mathcal{I}^1(\tilde{w}_{j,r}^n)\|_{L^2(K_l^n)}^2 dt \\
&\leq \mathcal{C}_1^2 \max_{x \in K_l^n} L(x) (h_l^n)^2 \sum_{r=0}^q \sum_{j=1}^{m_n} |\tilde{w}_{j,r}^n|_{H^1(\tilde{K}_l^n)}^2 \|t^r\|_{L^2(I_n)}^2, \tag{40}
\end{aligned}$$

where $\mathcal{D}(x, \psi_x^{-1}(\hat{y})) = L(x)^{-1}$ denotes the Jacobian associated with the map ψ_x , and with $\hat{\gamma}_1$ the reference fiber for the two-dimensional setting. Via this estimate, we obtain the following bound for the term (I) in (38):

$$\begin{aligned}
(\text{I}) &\leq k_n \|r_{R_l^n} - \bar{r}_{R_l^n}\|_{L^2(S_{R_l^n})} \left\| \frac{\partial(z_{\mathbf{m}} - z_{\mathbf{m}}^h)}{\partial t} \right\|_{L^2(S_{R_l^n})} \tag{41} \\
&\quad + \mathcal{C} \|\bar{r}_{R_l^n}\|_{L^2(S_{R_l^n})} h_l^n \left(\max_{x \in K_l^n} L(x) \right)^{\frac{1}{2}} \sum_{r=0}^q \sum_{j=1}^{m_n} |\tilde{z}_{j,r}^n - \tilde{z}_{j,r}^{n,h}|_{H^1(\tilde{K}_l^n)} \|t^r\|_{L^2(I_n)},
\end{aligned}$$

with \mathcal{C} a constant depending on \mathcal{C}_1 in (34), q and m_n . From now on, \mathcal{C} denotes a constant whose value may change from line to line. Term (II) can

be bounded analogously to contribution (I), by restricting the computations on the lateral surface $L_{R_l^n}$ of $S_{R_l^n}$. This yields

$$\begin{aligned} \text{(II)} &\leq \frac{k_n}{2} \|j_{R_l^n} - \bar{j}_{R_l^n}\|_{L^2(L_{R_l^n})} \left\| \frac{\partial(z_{\mathbf{m}} - z_{\mathbf{m}}^h)}{\partial t} \right\|_{L^2(L_{R_l^n})} \\ &+ \frac{1}{2} \|\bar{j}_{R_l^n}\|_{L^2(L_{R_l^n})} \| (z_{\mathbf{m}} - z_{\mathbf{m}}^h - \mathcal{I}^1(z_{\mathbf{m}} - z_{\mathbf{m}}^h)) \|_{L^2(L_{R_l^n})}. \end{aligned} \quad (42)$$

Inequality (40) is replaced by a corresponding trace estimate, obtained essentially by invoking result (35) instead of (34), to have

$$\|w_{\mathbf{m}} - \mathcal{I}^1(w_{\mathbf{m}})\|_{L^2(L_{R_l^n})}^2 \leq \mathcal{C}_2^2 \max_{x \in K_l^n} L(x) h_l^n \sum_{r=0}^q \sum_{j=1}^{m_n} \|\tilde{w}_{j,r}^n\|_{H^1(\tilde{K}_l^n)}^2 \|t^r\|_{L^2(I_n)}^2, \quad (43)$$

for any $w_{\mathbf{m}} \in V_{\mathbf{m}}^N$. Combining this result with (42), we attain the following control for the second term in (38):

$$\begin{aligned} \text{(II)} &\leq \frac{k_n}{2} \|j_{R_l^n} - \bar{j}_{R_l^n}\|_{L^2(L_{R_l^n})} \left\| \frac{\partial(z_{\mathbf{m}} - z_{\mathbf{m}}^h)}{\partial t} \right\|_{L^2(L_{R_l^n})} \\ &+ \frac{1}{2} \mathcal{C} \|\bar{j}_{R_l^n}\|_{L^2(L_{R_l^n})} (h_l^n)^{\frac{1}{2}} \left(\max_{x \in K_l^n} L(x) \right)^{\frac{1}{2}} \sum_{r=0}^q \sum_{j=1}^{m_n} \|\tilde{z}_{j,r}^n - \tilde{z}_{j,r}^{n,h}\|_{H^1(\tilde{K}_l^n)} \|t^r\|_{L^2(I_n)}, \end{aligned}$$

where constant \mathcal{C} depends on \mathcal{C}_2 in (35), q and m_n . We focus now on term (III) and, first of all, we apply again splitting (39):

$$\begin{aligned} \text{(III)} &\leq \left| \int_{R_l^n} \mathcal{J}_{n-1} [z_{\mathbf{m}} - z_{\mathbf{m}}^h - T_n(z_{\mathbf{m}} - z_{\mathbf{m}}^h)]^{n-1,+} dR_l^n \right| \\ &+ \left| \int_{R_l^n} \mathcal{J}_{n-1} [T_n(z_{\mathbf{m}} - z_{\mathbf{m}}^h - \mathcal{I}^1(z_{\mathbf{m}} - z_{\mathbf{m}}^h))]^{n-1,+} dR_l^n \right|. \end{aligned}$$

Now, thanks to the mean value theorem, we remark that, for any function $w_{\mathbf{m}} \in V_{\mathbf{m}}^n$,

$$(w_{\mathbf{m}} - T_n(w_{\mathbf{m}}))^{n-1,+} = w_{\mathbf{m}}^{n-1,+} - w_{\mathbf{m}}(t_n^*) = - \int_{t_{n-1}}^{t_n^*} \frac{\partial w_{\mathbf{m}}}{\partial t}(s) ds \quad (44)$$

with $t_n^* \in (t_{n-1}, t_n)$, as well as equality $\|\mathcal{J}_{n-1}\|_{L^2(S_{R_l^n})} = k_n^{\frac{1}{2}} \|\mathcal{J}_{n-1}\|_{L^2(R_l^n)}$ trivially holds. Moving from these results and by exploiting the definition of the projection operator T_n , the Cauchy-Schwarz inequality and estimate

(40), we derive the final bound for (III):

$$\begin{aligned}
\text{(III)} &\leq \left| \int_{S_{R_l^n}} \mathcal{J}_{n-1} \frac{\partial(z_{\mathbf{m}} - z_{\mathbf{m}}^h)}{\partial t} dR_l^n dt \right| \\
&+ \frac{1}{k_n} \left| \int_{S_{R_l^n}} \mathcal{J}_{n-1} \left(z_{\mathbf{m}} - z_{\mathbf{m}}^h - \mathcal{I}^1(z_{\mathbf{m}} - z_{\mathbf{m}}^h) \right) dR_l^n dt \right| \\
&\leq k_n^{\frac{1}{2}} \|\mathcal{J}_{n-1}\|_{L^2(R_l^n)} \left\| \frac{\partial(z_{\mathbf{m}} - z_{\mathbf{m}}^h)}{\partial t} \right\|_{L^2(S_{R_l^n})} \\
&+ \frac{1}{k_n^{\frac{1}{2}}} \|\mathcal{J}_{n-1}\|_{L^2(R_l^n)} \|z_{\mathbf{m}} - z_{\mathbf{m}}^h - \mathcal{I}^1(z_{\mathbf{m}} - z_{\mathbf{m}}^h)\|_{L^2(S_{R_l^n})} \\
&\leq \|\mathcal{J}_{n-1}\|_{L^2(R_l^n)} \left\{ k_n^{\frac{1}{2}} \left\| \frac{\partial(z_{\mathbf{m}} - z_{\mathbf{m}}^h)}{\partial t} \right\|_{L^2(S_{R_l^n})} \right. \\
&+ \left. \frac{\mathcal{C}}{k_n^{\frac{1}{2}}} \left(\max_{x \in K_l^n} L(x) \right)^{\frac{1}{2}} h_l^n \sum_{r=0}^q \sum_{j=1}^{m_n} |\tilde{z}_{j,r}^n - \tilde{z}_{j,r}^{n,h}|_{H^1(\tilde{K}_l^n)} \|t^r\|_{L^2(I_n)} \right\},
\end{aligned}$$

with \mathcal{C} as in (41). The last term in (38) can be controlled by repeating the same computations adopted for (III), by replacing the temporal residual \mathcal{J}_{n-1} with the initial error $e_{\mathbf{m}}^{h,0,-}$ and by focusing on the first time interval. We achieve the following estimate

$$\begin{aligned}
\text{(IV)} &\leq \|e_{\mathbf{m}}^{h,0,-}\|_{L^2(R_l^1)} \left\{ k_1^{\frac{1}{2}} \left\| \frac{\partial(z_{\mathbf{m}} - z_{\mathbf{m}}^h)}{\partial t} \right\|_{L^2(S_{R_l^1})} \right. \\
&+ \left. \frac{\mathcal{C}}{k_1^{\frac{1}{2}}} \left(\max_{x \in K_l^1} L(x) \right)^{\frac{1}{2}} h_l^1 \sum_{r=0}^q \sum_{j=1}^{m_n} |\tilde{z}_{j,r}^1 - \tilde{z}_{j,r}^{1,h}|_{H^1(\tilde{K}_l^1)} \|t^r\|_{L^2(I_1)} \right\},
\end{aligned}$$

with \mathcal{C} as in (43). Now, result (36) follows by properly combining the individual estimates obtained for terms (I)-(IV). \square

Moving from (36), we propose as error estimator for the discretization contribution in (24) the value

$$\eta^h = \sum_{n=1}^N \sum_{l=1}^{\mathcal{M}_n} \left[\rho_{R_l^n}^S(u_{\mathbf{m}}^h) \omega_{R_l^n}^S(z_{\mathbf{m}} - z_{\mathbf{m}}^h) + \sum_{i=1}^2 \rho_{R_l^n}^{Ti}(u_{\mathbf{m}}^h) \omega_{R_l^n}^{Ti}(z_{\mathbf{m}} - z_{\mathbf{m}}^h) \right], \quad (45)$$

so that the estimator for the global functional error, $|J(\varepsilon_{\mathbf{m}}^h)|$, coincides with $\eta_{\mathbf{mm}^+}^h = \eta_{\mathbf{mm}^+} + \eta^h$, with $\eta_{\mathbf{mm}^+}$ as in (19). In particular, since it is straightforward to distinguish in η^h the space from the time contribution given by

$$\eta_S^h = \sum_{n=1}^N \sum_{l=1}^{\mathcal{M}_n} \rho_{R_l^n}^S(u_{\mathbf{m}}^h) \omega_{R_l^n}^S(z_{\mathbf{m}} - z_{\mathbf{m}}^h), \quad \eta_T^h = \sum_{n=1}^N \sum_{l=1}^{\mathcal{M}_n} \sum_{i=1}^2 \rho_{R_l^n}^{Ti}(u_{\mathbf{m}}^h) \omega_{R_l^n}^{Ti}(z_{\mathbf{m}} - z_{\mathbf{m}}^h),$$

respectively, it is immediate to decompose $\eta_{\mathbf{mm}+}^h$ into a modeling, a space and a time contribution, as

$$\eta_{\mathbf{mm}+}^h = \eta_{\mathbf{mm}+} + \eta_S^h + \eta_T^h. \quad (46)$$

This splitting will be crucial with a view to the global adaptive procedure. Both the estimators η_S^h and η_T^h share the structure characterizing a goal-oriented analysis, i.e., they coincide with the product of a residual depending on the primal solution and a weight related to the dual solution. In addition, we remark that the HiMod procedure produces an evident effect in the definition of the weights, where the contribution along the x - and y -direction is split.

Some computational remarks on estimator η^h are now in order. To make computable the weights, we replace the dual solution $z_{\mathbf{m}}$ with a computable discrete counterpart $z_{\mathbf{m}}^{*,h}$. A possibility is to resort to the discrete enriched dual solution $z_{\mathbf{m}+}^h$. Nevertheless, since the temporal weights involve the time derivative of $z_{\mathbf{m}}$, we resort to a temporal recovery procedure yielding an approximation $z_{\mathbf{m}}^{*,h}$ that is at least linear in time. In particular, we follow the approach in [24, 25].

The dependence of the weights on the dual discretization error rather than on the dual solution is optimal in terms of convergence. Moreover, the time averaged residuals $\bar{r}_{R_t^n}$ and $\bar{j}_{R_t^n}$ make the estimator more reliable since $\|\bar{w}\|_{L^2(I_n)} \leq \|w\|_{L^2(I_n)}$ as well as $\|w - \bar{w}\|_{L^2(I_n)} \leq \|w\|_{L^2(I_n)}$ for any function $w \in L^2(I_n)$.

An extra care has to be devoted to the computation of the temporal residual \mathcal{J}_{n-1} that combines solutions associated with two different meshes. We use an interpolation operator from the degrees of freedom of \mathcal{T}_{h_n} onto the ones associated with $\mathcal{T}_{h_{n+1}}$.

Finally, the analysis in Proposition 4 may be generalized to a 3D framework provided that map ψ_x is properly chosen. In particular, the orthonormality of basis \mathcal{B} may be exploited to derive estimates (40) and (43) only if $\mathcal{D}^{-1}(x, \psi_x^{-1}(\hat{\mathbf{y}}))$ does not depend on $\hat{\mathbf{y}}$. This has to be explicitly demanded in a 3D setting while it always holds in a 2D framework.

5.2 Building the space-time adaptive HiMod lookup diagram

The goal of this section coincides with the one pursued via model adaptation, i.e., to keep the global functional error below a fixed tolerance TOL via an automatic selection of the modal distribution and now also of the space-time mesh $\{(K_l^n, I_n)_{l=1}^{M_n}\}_{n=1}^N$.

Different strategies are followed in the literature to combine model with mesh adaptation [37, 20, 16, 10]. The approach we propose iteratively alternates model with space-time mesh adaptation, by advantageously exploiting

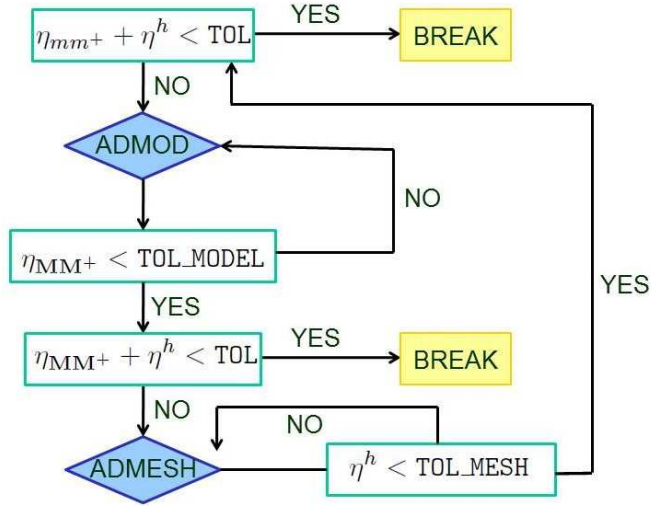


Figure 9: Flowchart of the global adaptive procedure.

the additive structure of the global error estimator in (46). For this reason, we distinguish a model (TOL_MODEL) and a mesh (TOL_MESH) tolerances, such that $TOL_MODEL + TOL_MESH = TOL$. Then, we follow the procedure outlined in Figure 9. We distinguish two main modules, ADMOD devoted to model adaptation and ADMESH dealing with the space-time mesh adaptation. The module ADMOD exactly implements the five-stage adaptive procedure previously described. Concerning the space-time mesh adaptation, the algorithm set by ADMESH is very straightforward, due to the one-dimensional nature of both the spatial and temporal meshes. In particular, while the space adaptation includes both mesh refinement (via bisection) and coarsening (gluing two consecutive intervals where η_S^h is below tolerance), the time adaptive algorithm deals only with mesh refinement. This suggests to start the adaptive procedure on a sufficiently coarse time partition. Error equidistribution drives both the space and time adaptation. A maximum value constrains the number of iterations as well as tuning parameters δ_{1H} ($= 0.5$), δ_{2H} ($= 1.5$) limit the spatial mesh refinement and coarsening to the worst and to the best subintervals, respectively.

As highlighted in Figure 9, after a preliminary check on the accuracy of the global error estimator associated with the initial uniform modal distribution and the initial uniform space-time grid, model adaptation takes place till the accuracy TOL_MODEL is matched by estimator η_{MM+} . Then, we check if model adaptation suffices to provide the global tolerance TOL without any space-time mesh adaptation. If not the module ADMESH is activated. In particular, we apply the spatial rather than temporal adaptation depending on which of the estimators η_S^h , η_T^h is the greatest one. When $\eta^h < TOL_MESH$, we

come back to the initial check on the global accuracy.

A maximum number of iterations ensures the end of the whole adaptive procedure. We remark that each time the space-time partition is updated, a projection of the primal and dual solutions involved in the evaluation of the error estimator is demanded. As for the choice of the tolerances, we opted for a convex combination of the different tolerances, by selecting $\text{TOL_MODEL} = \theta \text{TOL}$ and $\text{TOL_MESH} = (1 - \theta) \text{TOL}$, with $0 \leq \theta \leq 1$ [10]. The parameter θ settles a relation between model and discretization error, in accordance with requirement (22).

Finally, we refer to the outcome of the whole adaptive algorithm as to the space-time adaptive HiMod lookup diagram. Some instances of this table are provided in the next section.

5.3 Numerical verification of the space-time adaptive HiMod diagram

The test case used to validate the modeling adaptive procedure for $J = J_{\text{mean},T}$ is now tackled by activating the mesh adaptation as well. We preserve the same values of the previous run for tolerance TOL, for the initial uniform modal indices m and m^+ , and for the initial space-time mesh. Then, we set $\theta = 0.5$.

The adaptive procedure converges after 50 iterations, i.e., 23 model iterations followed by 9 and 8 adaptations of the spatial and of the temporal mesh, respectively and by 10 additional model adaptations. The final outcome of the offline phase is the HiMod lookup diagram in Figure 10, top-left. A comparison between this table and the one in Figure 7, left shows a similar trend for the number of modes, i.e., a gradual increment of the number of modes as we approach the final time and in correspondence with the source location and the downstream areas. Nevertheless, the combination of model with mesh adaptation reduces from 3 to 1 the number of modes used in the first phase of the test case (compare Figure 7, center with Figure 11, left). Concerning the spatial adaptation, a coarse mesh consisting of less than 20 subintervals and refined around $x = 1.5$ is predicted for the first time intervals. Then, this number increases with an abrupt variation in the last time interval when it reaches its maximum (see Figure 11, center). The monotone trend characterizing the model and the spatial mesh adaptation is qualitatively the same, exhibiting a refinement of the modes and of the finite element partition confined to the last time intervals, in accordance with the goal quantity.

On the contrary, the time adaptation yields a non monotone prediction for the time step distribution, as depicted in Figure 11, right. Essentially we recognize two phases when the initial time step is considerably reduced, the first one around the initial time and the second one just before time T . A strong refinement of the initial grid is recurrent in mesh adaptation and here

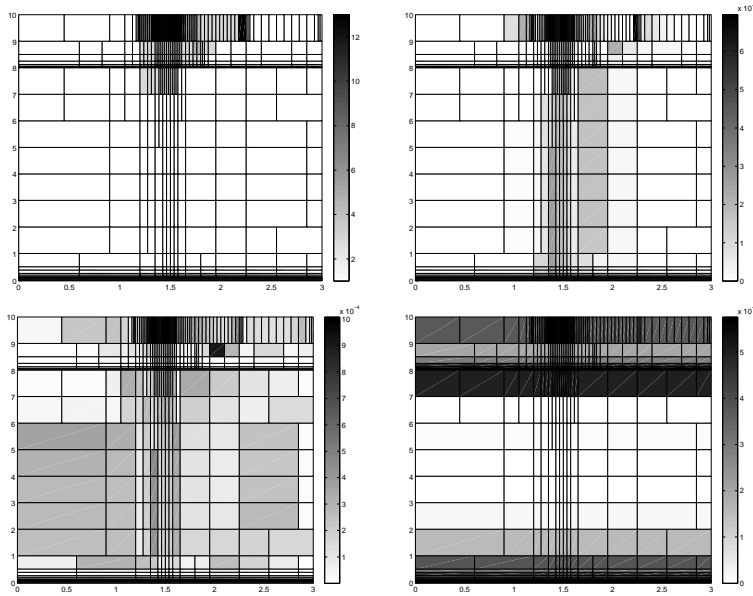


Figure 10: Convection-diffusion of a pollutant, control of $J_{\text{mean},T}$, global adaptation: space-time adaptive HiMod lookup diagram (top-left); space-time distribution of η_{MM^+} (top-right), of η_S^h (bottom-left) and of η_T^h (bottom-right).

it likely balances the initial rough modal and spatial discretizations. The second refinement occurs when the control of the mean value becomes more relevant. At time $t = 0.8$, both the modal discretization and the space-time mesh are considerably refined to ensure the imposed tolerance. Probably, a complex interplay among the three discretizations takes place during the last time intervals, so that the severe demand on the time step is relaxed again before reaching the final time.

Figure 10 gathers the values of the three error estimators distributed on the space-time lookup diagram. The choice made for the tolerances leads to values of the same order of magnitude for η_{MM^+} and η_S^h , while the error estimator associated with the time discretization assumes larger values.

As shown in Figure 12, the $\text{c}[\text{M}(\mathbf{M})\text{G}(1)]\text{-dG}(0)$ HiMod solution generated by the online phase starting from the diagram in Figure 10, top-left is qualitatively different from the one in Figure 6, right. The adoption of a single mode till $t = 0.7$ identifies a reduced solution which is initially very far from the full one. Nevertheless, the time steps predicted by the adaptive algorithm are enough to refine, during the last time intervals, the number of modes as well as the partition along Ω_{1D} so that solution $u_{\mathbf{M}}^h$ becomes fully comparable with the full one at the final time.

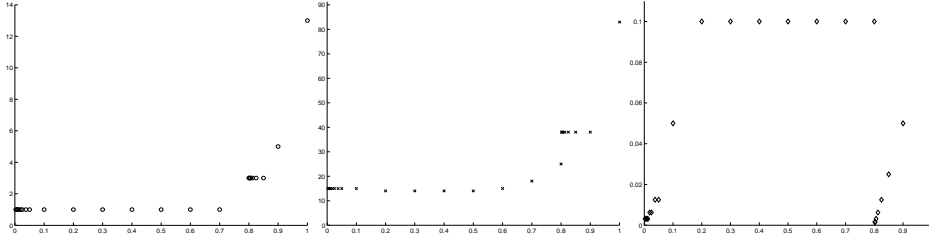


Figure 11: Convection-diffusion of a pollutant, control of $J_{\text{mean},T}$, global adaptation: modal distribution at $x=1.5$ as a function of time (left); mesh cardinality (center) and time-step (right) evolution.

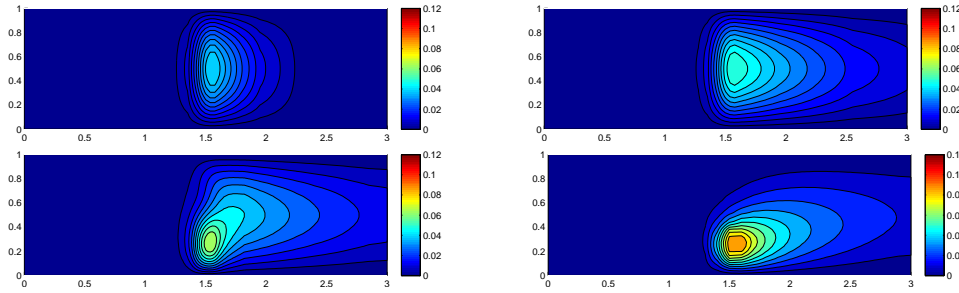


Figure 12: Convection-diffusion of a pollutant, control of $J_{\text{mean},T}$, global adaptation: HiMod approximation u_M^h at $t = 0.1, 0.2, 0.8, 1$ (top-bottom, left-right).

5.3.1 Neumann boundary conditions

We challenge the whole adaptive procedure by modifying the boundary conditions in the previous test case. We assign a homogeneous Neumann condition on the whole boundary, except for the edge $\Gamma_D = \{(0, y) : 0 \leq y \leq 1\}$ where we preserve the homogeneous Dirichlet datum. The new condition along the horizontal sides leads to select a new modal basis. After identifying the reference fiber $\hat{\gamma}_1$ with the interval $[0, 1]$, we choose $\mathcal{B} = \{\varphi_j(\hat{y}) = \sqrt{2} \cos(\pi j \hat{y})\}_{j \in \mathbb{N}}$.

Figure 13, left shows the cG(1)-dG(0) full solution at four different times, computed on a uniform unstructured mesh of 10252 elements. In particular, the new flux-free configuration erases the horizontal dynamics in Figure 6, pushing the pollutant to contaminate also the northeast and the southeast areas. If we set the global adaptive procedure to control $J_{\text{mean},T}$, we do not expect much benefit from the modal basis since all the cosine functions have a null mean except φ_0 . Figure 14, top and Figure 15, top-left collect some results of the global adaptive procedure for $\text{TOL_MODEL}=\text{TOL_MESH}= 5 \cdot 10^{-3}$. The adaptive algorithm stops after 10 iterations. No model adaptation is performed and only function φ_0 is switched on. On the contrary, both the

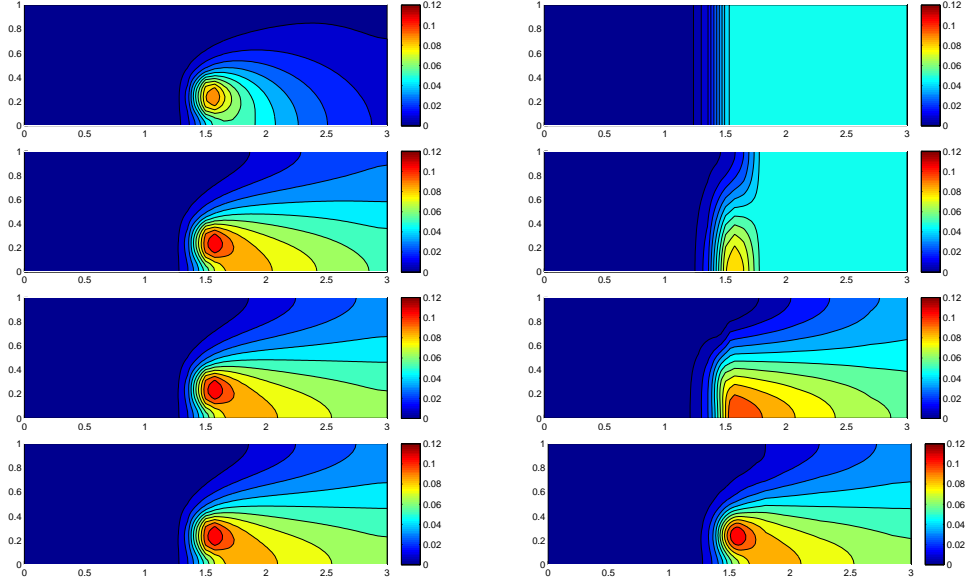


Figure 13: Convection-diffusion of a pollutant, control of $J_{\text{mean},T}^{\text{down}}$, global adaptation: full solution (left) and pointwise HiMod approximation $u_{\mathbf{M}}^h$ (right), at $t = 0.1, 0.5, 0.8, 1$ (top-bottom).

spatial and the temporal meshes are adapted via 7 and 3 iterations, respectively. The cardinality of the finite element mesh reaches a minimum in the middle of the interval I , while, after an initial refinement, the time step increases to the initial value 0.1. Overall, the modal-space-time discretization is coarse as shown by the HiMod lookup diagram. The $c[\mathbf{M}(\mathbf{M})\mathbf{G}(1)]\text{-dG}(0)$ HiMod solution generated in the online phase is provided in Figure 15, bottom for two different times. It is not surprising that $u_{\mathbf{M}}^h$ loses the essential features of the full solution due to the deficiency of the reduced model. Smaller values of TOL, of course, do not modify this trend.

A completely different prediction is performed by changing the goal functional J into $J_{\text{mean},T}^{\text{down}} = [\text{meas}(\Omega^{\text{down}})]^{-1} \int_{\Omega^{\text{down}}} \zeta(x, y, 1) d\Omega^{\text{down}}$, with $\Omega^{\text{down}} = (0, 3) \times (0, 0.5)$. The global tolerance TOL = 10^{-2} is now guaranteed after 30 model iterations, followed by 7 spatial and 9 temporal mesh adaptations, plus a final model adaptation. The space-time adaptive HiMod lookup diagram yielded by the offline phase is shown in Figure 15, top-right. The number of cosine functions is gradually increased to eight in correspondence with \mathcal{D} . Additional modes are now demanded also upstream the source location in contrast to Figure 10, top-left. The modal as well as the spatial mesh cardinality trend is very similar to the one in Figure 11, whereas three refinements of the time step now occur (see Figure 14). The additional refinement about in the middle of the time window corresponds to the phase when the pointwise HiMod solution starts to become similar to

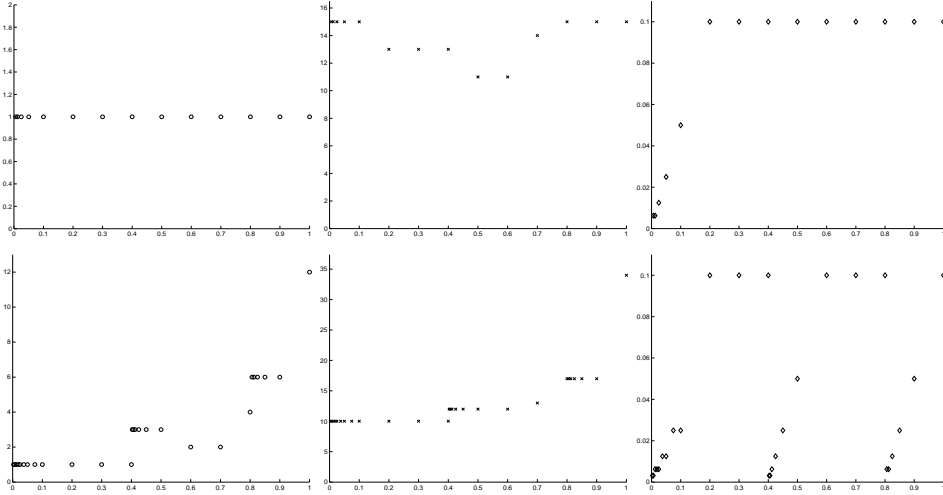


Figure 14: Convection-diffusion of a pollutant, global adaptation: space-time distribution of η_{MM+} (left), of η_S^h (center) and of η_T^h (right), for $J_{\text{mean},T}$ (top) and $J_{\text{mean},T}^{\text{down}}$ (bottom).

the full one. Indeed, as shown in Figure 13, right solution u_M^h is initially far from the full one (and similar to the pointwise approximation in Figure 15). Then, from $t = 0.5$, u_M^h becomes more and more similar to the full solution till, at the final time, the two solutions are almost identical.

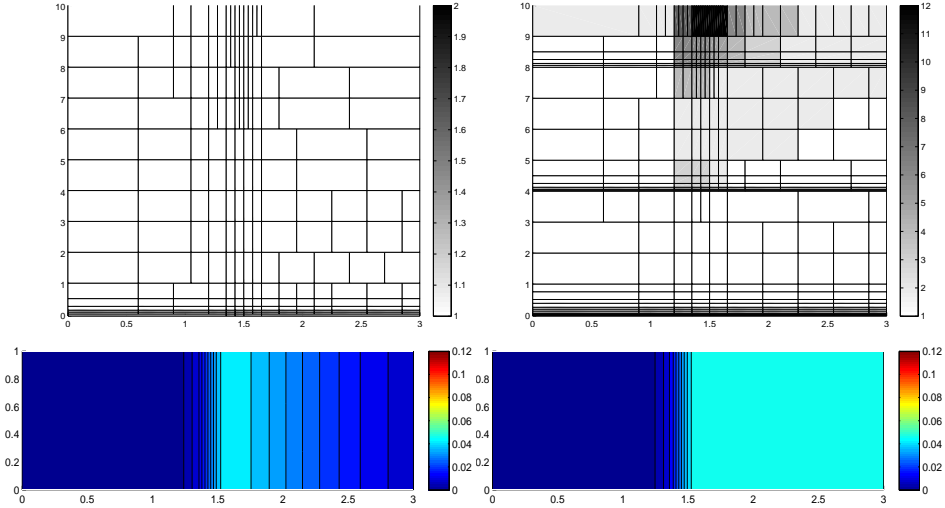


Figure 15: Convection-diffusion of a pollutant, global adaptation: space-time adaptive HiMod lookup diagram (top) associated with $J_{\text{mean},T}$ (left) and $J_{\text{mean},T}^{\text{down}}$ (right); pointwise HiMod approximation associated with $J_{\text{mean},T}$ (bottom) at $t = 0.2$ (left) and $t = 1$ (right).

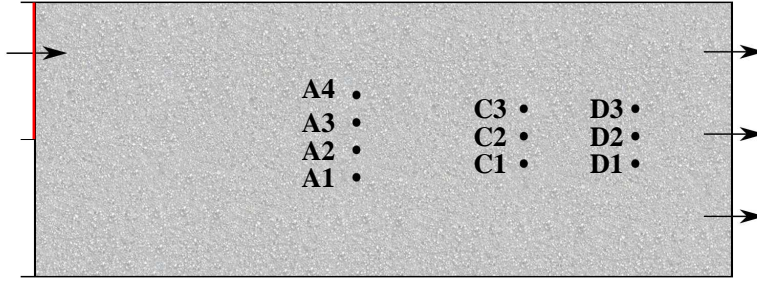


Figure 16: Diagram of the experimental configuration used for the validation.

6 Validation of the HiMod reduction

This is a first attempt of validation for the HiMod reduction procedure. For this purpose, we focus on the experimental and modeling analysis provided in [26] dealing with a reactive transport in homogeneous porous media.

We consider the experimental setting outlined in Figure 16. It consists of a rectangular laboratory flow cell of dimension $2.5\text{dm} \times 1\text{dm} \times 0.08\text{dm}$ along the x -, y - and z -direction, respectively. The cell is filled with a porous media with measured porosity equal to 0.375 and it is initially saturated with an aqueous solution. Segment $\Gamma_{\text{inlet}} = \{(0, y, z) : 0.5 \leq y \leq 1, 0 \leq z \leq 0.08\}$ coincides with an inlet boundary, where a constant concentration, modeling the injection of a reactive component, is assigned. Simultaneously, a flow rate of 12ml/h is set at the outlet $\Gamma_{\text{outlet}} = \{(2.5, y, z) : 0 \leq y \leq 1, 0 \leq z \leq 0.08\}$, resulting in an average water velocity of about 0.404dm/h at the equilibrium. We remark that the set-up of the experiment is designed to have a pseudo-1D flow, parallel to the x -axis. Finally, ten sampling ports are located in the cell, to collect measurements of the reactive fluid concentration. Sampling is performed four times during each experiment. The concentration measurements represent the data we aim at matching via a HiMod reduced modeling in the same spirit of the analysis in [26]. The reactive transport experiment is conducted for 60 hours, though a stationary state is reached already after 15 hours from the beginning of the experiment, so that we restrict the time window of investigation to $(0, 30)$.

For all the further experimental data we refer to [26] since a greater level of detail on the experimental setting is beyond the purposes of the paper.

From a modeling viewpoint, since the setting is invariant along the z -axis, we can simulate the experiment in an effective way as a two-dimensional

flow. In particular, we adopt the unsteady equation

$$\left\{ \begin{array}{l} \frac{\partial u}{\partial t}(x, y, t) - 0.00085 \Delta u(x, y, t) + 0.404 \frac{\partial u}{\partial x}(x, y, t) = 0 \quad (x, y, t) \in \Omega \times (0, 30) \\ \frac{\partial u}{\partial y}(x, 0, t) = \frac{\partial u}{\partial y}(x, 1, t) = 0 \quad 0 \leq x < 2.5, t \in (0, 30) \\ u(0, y, t) = 0 \quad 0 \leq y < 0.5, t \in (0, 30) \\ u(0, y, t) = 0.045 \quad 0.5 \leq y < 1, t \in (0, 30) \\ \frac{\partial u}{\partial x}(3, y, t) = 0 \quad 0 \leq y < 1, t \in (0, 30) \\ \frac{\partial u}{\partial x}(x, y, 0) = 0 \quad (x, y) \in \Omega, \end{array} \right. \quad (47)$$

with $\Omega = (0, 2.5) \times (0, 1)$, to model the process of advection and diffusion of the reactive component. Notice that (47) represents a simplified version of the original model in [26]. A preliminary tuning of the model parameters has been carried out to make the solution of the two models as close as possible in the considered experimental context. In more detail, we adopt a constant diffusive coefficient whose value is set, via a trial and error procedure, to replicate the action of the diffusive tensor used in [26]. Moreover, following [26], we select the value for the flux velocity by solving an additional Darcy problem.

Figure 17, left shows the full solution computed on a uniform unstructured mesh of 13078 triangles at $t = 5\text{h}, 11\text{h}, 15\text{h}, 19\text{h}$. The reactive fluid gradually spreads into the flow cell and reaches the stationary stage.

We now test the HiMod reduction procedure. We first resort to a uniform HiMod approximation and we use 20 modal functions to describe the transverse dynamics. We adopt a uniform space-time discretization along Ω_{1D} and $(0, 30)$, with step $h = 0.05$ and $k = 0.5$, respectively. In Figure 17, right we gather the HiMod solution u_{20}^h at $t = 5\text{h}, 11\text{h}, 15\text{h}, 19\text{h}$. The reliability of the reduced solution is satisfactory, despite the complexity of the phenomenon and the confined number of modal function. Now, we focus on the actual validation phase. For this purpose, in Figure 18, we compare the simulated (diamond symbols) with the measured (circle symbols) concentrations in correspondence with eight of the ten sampling ports in Figure 16. We refer only to one of the two sets of data available in [26]. The agreement between simulated and measured concentrations is very good. The prediction provided by the HiMod approximation is fully comparable with the one of Figure 3 in [26]. In particular, while the results at ports A1, A2, C1, D1 are very similar, we detect an improvement in the concentrations predicted by the HiMod reduction procedure at ports A3 and C3, probably due to the cut-off of the high frequencies. Qualitatively, at each port, we recognize a first phase of about 8 hours when the chemical breakthrough, characterized by a sigmoid shape curve, occurs; successively, the steady state is reached and each curve exhibits a plateau.

As last test, we assess the reliability of the modeling adaptive procedure

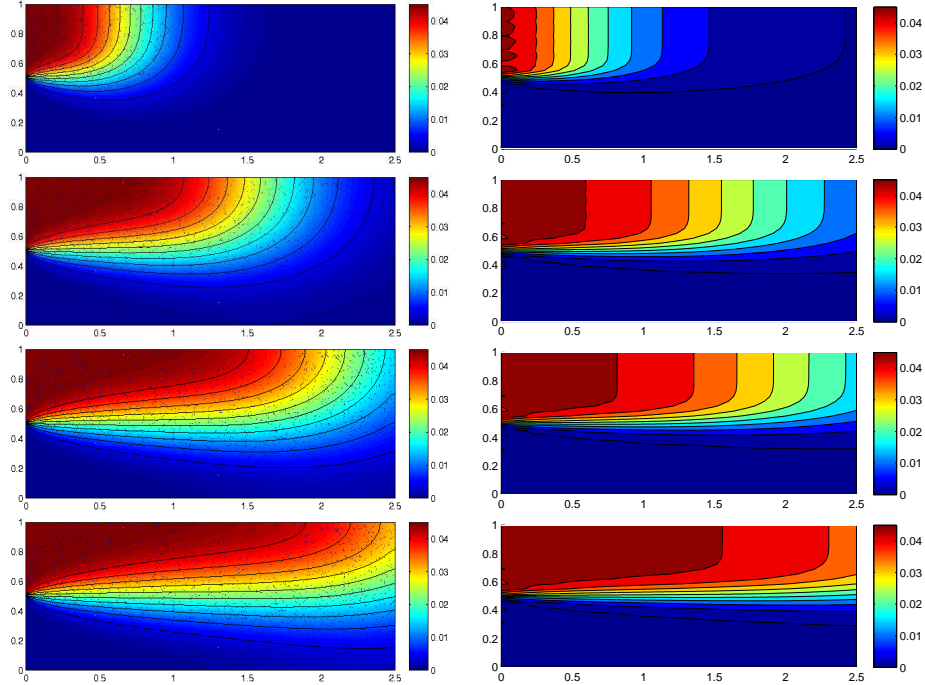


Figure 17: Reactive transport in porous media: full solution (left) and uniform HiMod approximation u_{20}^h (right) at $t = 5\text{h}, 11\text{h}, 15\text{h}, 19\text{h}$ (top-bottom).

in a validation context. We aim at evaluating the reactive fluid concentration at $\tilde{t} = 15\text{h}$ via the $c[\text{M}(\text{M})\text{G}(1)]\text{-dG}(0)$ HiMod solution predicted by the modeling adaptive procedure. We consequently choose functional J as $J_{15}(\zeta) = [\text{meas}(\Omega)]^{-1} \int_{\Omega} \zeta(x, y, 15) d\Omega$. The expectation is to obtain a value for the concentration similar to the one provided by u_{20}^h and not so far from the experimental data, but via a HiMod solution computationally cheaper than u_{20}^h . This would confirm the desired trade-off between modeling reliability and computational efficiency. We set the adaptive algorithm with $\text{TOL} = 10^{-3}$, $m = 1$, $m^+ = 3$. Concerning the space-time discretization that is held fixed in the simulation, we adopt a uniform space-time subdivision of $\Omega_{1D} \times I$ with $h = 0.05$ and $k = 0.5$. Finally, we reduce the time window to $(0, 15)$ due to the stationary regime of the flow in the interval $(15, 30)$.

The modeling adaptive algorithm converges after 599 iterations. It returns the HiMod lookup diagram in Figure 19, left characterized by the space-time distribution of η_{MM^+} in Figure 19, right. Both the diagrams corroborate the complexity of this experiment. In contrast to a more localized phenomenon such as the convection-diffusion of a pollutant in the previous sections, the refinement of the number of modes now gradually involves the whole Ω_{1D} as we approach time \tilde{t} .

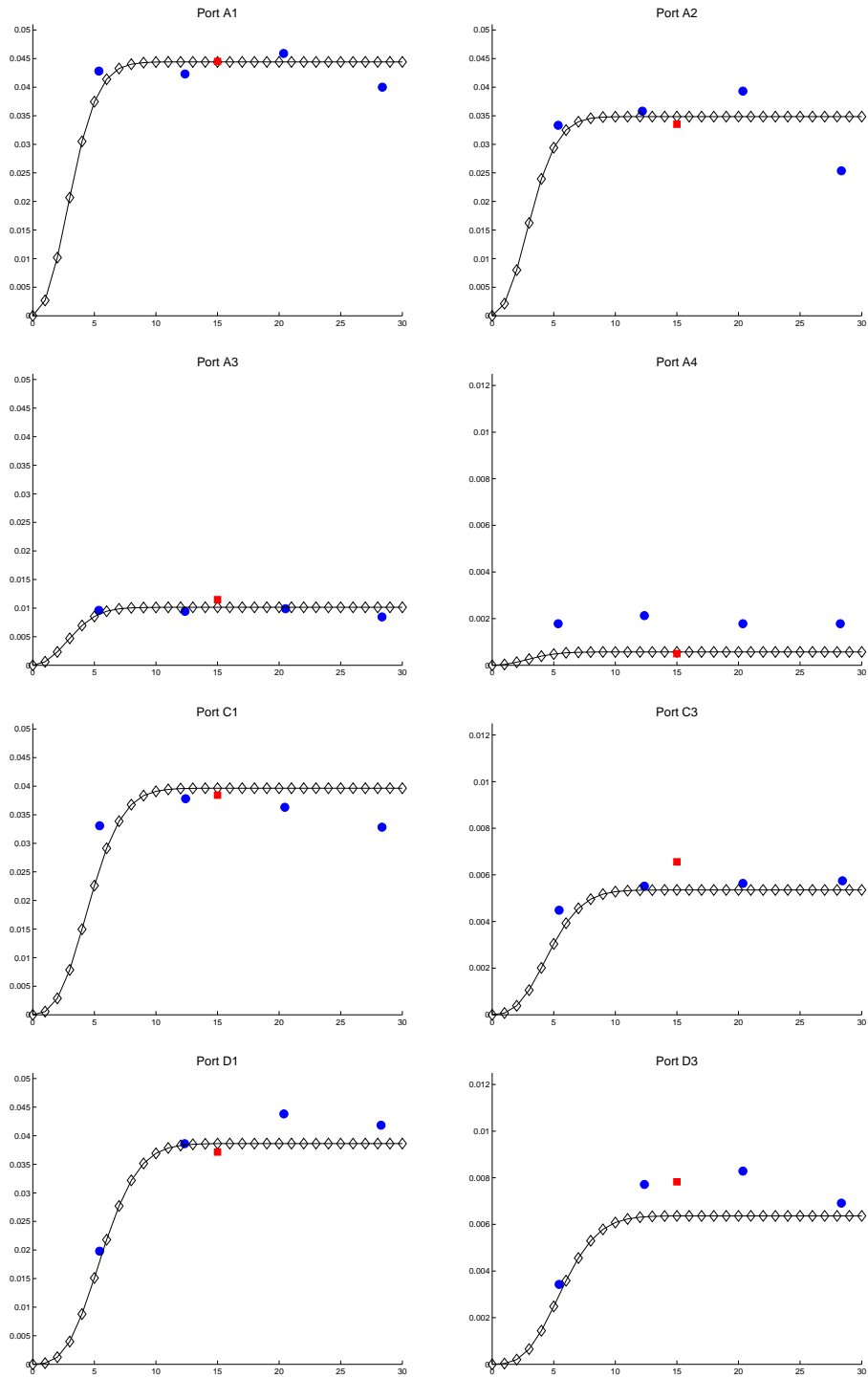


Figure 18: Reactive fluid concentrations at the sampling ports A1, A2, A3, A4, C1, C3, D1, D3 (top-bottom, left-right): measured (circle symbols) and simulated concentrations via u_{20}^h (diamond symbols) and via u_M^h (square symbols).

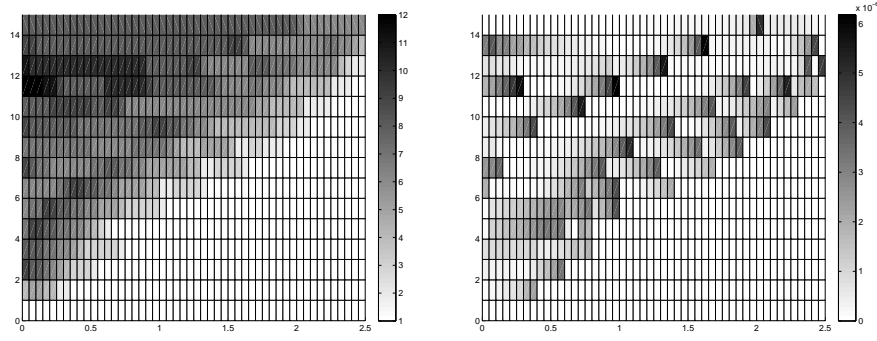


Figure 19: Reactive transport in porous media, control of J_{15} , modal adaptation: HiMod lookup diagram (left) and corresponding space-time distribution of η_{MM}^+ (right).

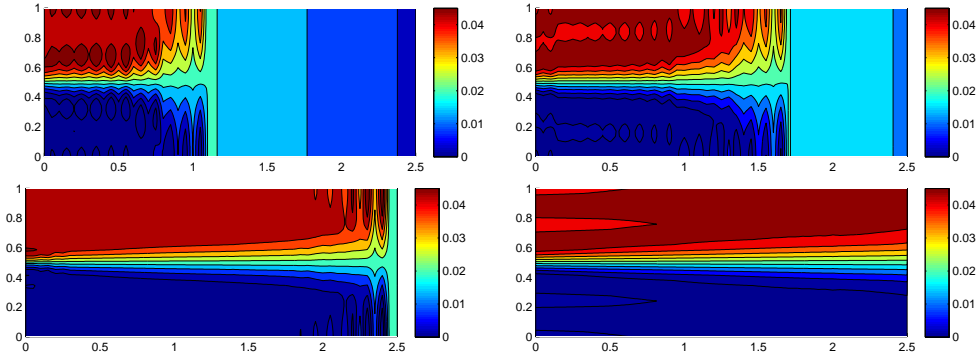


Figure 20: Reactive transport in porous media, control of J_{15} , modal adaptation: HiMod approximation at $t = 5h, 7h, 11h, 15h$ (top-bottom, left-right).

The non uniform trend of the estimator highlights the demanding work performed by the adaptive procedure to guarantee tolerance TOL. Despite these difficulties, the maximum number of modal functions required by the lookup diagram is 12 to be associated with the area closer to the inlet and with the time intervals immediately preceding the steady state. The point-wise HiMod approximation u_M^h generated by the online phase is depicted in Figure 20, for $t = 5h, 7h, 11h, 15h$. The trend of the adapted solution becomes more and more similar to the one in Figure 17, as t approaches \tilde{t} .

Finally, we examine the concentration values predicted by the adapted HiMod solution at $\tilde{t} = 15h$ in correspondence with the eight ports in Figure 18 (see the square symbols). It is evident the good matching of the simulated concentrations between u_{20}^h and u_M^h , with a slight different prediction at ports C3 and D3. In particular, the concentration computed by the adapted model at port D3 is closer to the experimental measurements with respect to the value provided by u_{20}^h .

7 Conclusions and perspectives

We have successfully extended the pointwise HiMod approach to an unsteady setting, by formalizing the so-called $c[M(\mathbf{M})G(s)]\text{-dG}(q)$ HiMod reduction procedure. The goal-oriented *a posteriori* error analysis has allowed us to devise an automatic algorithm to select the reduced model, that guarantees the desired accuracy on the functional of interest. The results yielded by the global adaptive procedure are very satisfying, despite the complex interplay among the three adaptations. This is confirmed by the HiMod lookup diagrams in Figure 10, top-left and Figure 15. The sensitivity of the predicted HiMod reduced model with respect to the goal quantity has been correctly validated as well (see, e.g., Figure 8 and Figure 15, bottom). Finally, the preliminary validation results in the last section are absolutely promising with a view to an effective application of HiMod to practical problems.

Prospective extensions of HiMod reduction include the approximation of nonlinear as well as 3D problems. This will be a crucial effort with a view to our last goal, i.e., to use HiMod reduction for the simulation of the blood flow in the arterial system.

Acknowledgments

The authors thank Giovanni Porta for the advices on the validation test case.

Moreover, the first author gratefully acknowledges the NSF project DMS 1419060 “Hierarchical Model Reduction Techniques for Incompressible Fluid-Dynamics and Fluid-Structure Interaction Problems” (P.I. Alessandro Veneziani) and the MIUR-PRIN 2010/2011 project “Innovative Methods for Water Resources under Hydro-Climatic Uncertainty Scenarios” for the financial support. The second author is partially supported by the ERC Advanced Grant 2013 n. 321186, “ReaDi, Reaction-Diffusion Equations, Propagation and Modeling” and by the project ERC Advanced Grant 2013 n. 339958, “Complex Patterns for Strongly Interacting Dynamical Systems, COMPAT”.

References

- [1] Lorenz, B., Biros, G., Ghattas, O., Heinkenschloss, M., Keyes, D., Mallick, B., Tenorio, L., van Bloemen Waanders, B., Willcox, K., Marzouk, Y. (eds.): Large-Scale Inverse Problems and Quantification of Uncertainty vol. 712. John Wiley & Sons, Chichester, West Sussex (2011)
- [2] Maday, Y., Ronquist, E.M.: A reduced-basis element method. C. R. Acad. Sci. Paris Ser. **I**(335), 195–200 (2002)

- [3] Kunisch, K., Volkwein, S.: Galerkin proper orthogonal decomposition methods for parabolic problems. *Numer. Math.* **148**, 117–148 (2001)
- [4] Chinesta, F., Ammar, A., Cueto, E.: Recent advances and new challenges in the use of the proper generalized decomposition for solving multidimensional models. *Arch. Comput. Methods Eng.* **17**(4), 327–350 (2010)
- [5] Blanco, P.J., Leiva, J.S., Feijóo, R.A., Buscaglia, G.C.: Black-box decomposition approach for computational hemodynamics: one-dimensional models. *Comput. Methods Appl. Mech. Engrg.* **200**(13-16), 1389–1405 (2011)
- [6] Formaggia, L., Quarteroni, A., Veneziani, A. (eds.): *Cardiovascular Mathematics, Modeling and Simulation of the Circulatory System. Modeling Simulation and Applications*, vol. 1. Springer, Milano (2009)
- [7] Bruckstein, A.M., Donoho, D.L., Elad, M.: From sparse solutions of systems of equations to sparse modeling of signal and images. *SIAM Review* **51**(1), 34–81 (2009)
- [8] Ern, A., Perotto, S., Veneziani, A.: Hierarchical model reduction for advection-diffusion-reaction problems. In: Kunisch, K., Of, G., Steinbach, O. (eds.) *Numerical Mathematics and Advanced Applications*, pp. 703–710. Springer, Berlin (2008)
- [9] Perotto, S., Ern, A., Veneziani, A.: Hierarchical local model reduction for elliptic problems: a domain decomposition approach. *Multiscale Model. Simul.* **8**(4), 1102–1127 (2010)
- [10] Perotto, S., Veneziani, A.: Coupled model and grid adaptivity in hierarchical reduction of elliptic problems. *J. Sci. Comput.* **60**(3), 505–536 (2014)
- [11] Perotto, S., Zilio, A.: Hierarchical model reduction: three different approaches. In: Cangiani, A., Davidchack, R., Georgoulis, E., Gorbunov, A., Levesley, J., Tretyakov, M. (eds.) *Numerical Mathematics and Advanced Applications*, pp. 851–859. Springer, Berlin (2013)
- [12] Perotto, S.: A survey of hierarchical model (Hi-Mod) reduction methods for elliptic problems. In: Idelsohn, S.R. (ed.) *Numerical Simulations of Coupled Problems in Engineering. Computational Methods in Applied Sciences*, vol. 33, pp. 217–241. Springer, Cham (2014)
- [13] Eriksson, K., Johnson, C., Thomée, V.: Time discretization of parabolic problems by the discontinuous Galerkin method. *RAIRO Modelisation Math. Anal. Numer.* **19**, 611–643 (1985)

- [14] Thomée, V.: Galerkin Finite Element Methods for Parabolic Problems, 2nd edn. Springer Series in Computational Mathematics, vol. 25. Springer, Berlin (2006)
- [15] Eriksson, K., Estep, D., Hansbo, P., Johnson, C.: Computational Differential Equations. Cambridge University Press, Cambridge (1996)
- [16] Micheletti, S., Perotto, S., David, F.: Model adaptation enriched with an anisotropic mesh spacing for nonlinear equations: application to environmental and CFD problems. *Numer. Math. Theor. Meth. Appl.* **6**(3), 447–478 (2013)
- [17] Becker, R., Rannacher, R.: An optimal control approach to a posteriori error estimation in finite element methods. *Acta Numer.* **10**, 1–102 (2001)
- [18] Giles, M.B., Süli, E.: Adjoint methods for PDEs: a posteriori error analysis and postprocessing by duality. *Acta Numer.* **11**, 145–236 (2002)
- [19] Oden, J.T., Prudhomme, S.: Goal-oriented error estimation and adaptivity for the finite element method. *Comput. Math. Appl.* **41**, 735–756 (2001)
- [20] Braack, M., Ern, A.: A posteriori control of modeling errors and discretization errors. *Multiscale Model Simul.* **1**, 221–238 (2003)
- [21] Stein, E., Rüter, M., Ohnimus, S.: Error-controlled adaptive goal-oriented modeling and finite element approximations in elasticity. *Comput. Methods Appl. Mech. Eng* **196**, 3598–3613 (2007)
- [22] Verfürth, R.: A posteriori error estimate for finite element discretizations of the heat equation. *Calcolo* **40**, 195–212 (2003)
- [23] Cascón, J.M., Ferragut, L., Asensio, M.I.: Space-time adaptive algorithm for the mixed parabolic problem. *Numer. Math.* **103**, 367–392 (2006)
- [24] Meidner, D., Vexler, B.: Adaptive space-time finite element methods for parabolic optimization problems. *SIAM J. Control Optim.* **46**(1), 116–142 (2007)
- [25] Micheletti, S., Perotto, S.: Space-time adaptation for purely diffusive problems in an anisotropic framework. *Int. J. Numer. Anal. Model.* **7**(1), 125–155 (2010)

- [26] Katz, G.E., Berkowitz, B., Guadagnini, A., Saaltink, M.W.: Experimental and modeling investigation of multicomponent reactive transport in porous media. *Journal of Contaminant Hydrology* **120-121**, 27–44 (2011)
- [27] Lions, J.-L., Magenes, E.: *Non Homogeneous Boundary Value Problems and Applications*. Springer, Berlin (1972)
- [28] Dautray, R., Lions, J.-L.: *Mathematical Analysis and Numerical Methods for Science and Technology: Evolution Problems I* vol. 5. Springer, Berlin (1992)
- [29] Perotto, S.: Hierarchical model (Hi-Mod) reduction in non-rectilinear domains. In: Erhel, J., Gander, M., Halpern, L., Pichot, G., T., S., Widlund, O. (eds.) *Lect. Notes Comput. Sci. Eng* vol. 98, pp. 477–485. Springer, Cham (2014)
- [30] Aletti, M., Perotto, S., Veneziani, A.: Educated bases for the hierarchical model (HiMod) reduction of advection-diffusion-reaction problems (2015). in preparation
- [31] Bellhouse, B.J., Bellhouse, F.H., Curl, C.M., MacMillan, T.I., Gunning, A.J., Spratt, E.H., MacMurray, S.B., Nelems, J.M.: A high efficiency membrane oxygenator and pulsatile pumping system and its application to animal trials. *Trans. Amer. Soc. Artif. Int. Organs* **19**, 72–79 (1973)
- [32] Bank, R.E., Smith, R.K.: A posteriori error estimates based on hierarchical bases. *SIAM J. Numer. Anal.* **30**, 921–935 (1993)
- [33] Dörfler, W., Nochetto, R.H.: Small data oscillation implies the saturation assumption. *Numer. Math.* **91**, 1–12 (2002)
- [34] Achchab, B., Achchab, S., Agouzal, A.: Some remarks about the hierarchical a posteriori error estimate. *Numer. Methods Partial Differential Equations* **20**(6), 919–932 (2004)
- [35] Griewank, A., Walther, A.: Algorithm 799: Revolve: an implementation of checkpointing for the reverse or adjoint mode of computational differentiation. *ACM T. Math. Software* **26**(1), 19–45 (2000)
- [36] Clément, P.: Approximation by finite element functions using local regularization. *RAIRO Anal.Numer.* **2**, 77–84 (1975)
- [37] Ainsworth, M.: A posteriori error estimation for fully discrete hierarchic models of elliptic boundary value problems on thin domains. *Numer. Math.* **80**, 325–362 (1998)

MOX Technical Reports, last issues

Dipartimento di Matematica
Politecnico di Milano, Via Bonardi 9 - 20133 Milano (Italy)

- 05/2015** Chen, P.; Quarteroni, A.; Rozza, G.
Reduced order methods for uncertainty quantification problems
- 1/2015** Pini, A.; Stamm, A.; Vantini, S.
Hotelling s T^2 in functional Hilbert spaces
- 2/2015** Menafoglio, A.; Petris, G.
Kriging for Hilbert-space valued random fields: the Operatorial point of view
- 3/2015** Abramowicz, K.; de Luna, S.; Häger, C.; Pini, A.; Schelin, L.; Vantini, S.
Distribution-Free Interval-Wise Inference for Functional-on-Scalar Linear Models
- 4/2015** Arioli, G.; Gazzola, F.
On a nonlinear nonlocal hyperbolic system modeling suspension bridges
- Antonietti, P. F.; Grasselli, M.; Stangalino, S.; Verani, M.
Discontinuous Galerkin approximation of linear parabolic problems with dynamic boundary conditions
- 62/2014** Andrà, C.; Parolini, N.; Verani, M.
Using gambling simulators to foster awareness about gambling risks
- 61/2014** Taffetani, M.; Ciarletta, P.
Elasto-capillarity controls the formation and the morphology of beads-on-string structures in solid fibres
- 58/2014** Menafoglio, A.; Secchi, P.; Guadagnini, A.
A Class-Kriging predictor for Functional Compositions with Application to Particle-Size Curves in Heterogeneous Aquifers
- 59/2014** Manzoni, A.; Pagani, S.; Lassila, T.
Accurate solution of Bayesian inverse uncertainty quantification problems using model and error reduction methods